Microvascular Research (USA)
https://www.journals.elsevier.com/microvascular-research
IMPACT FACTOR = 3.514

ACCEPTED SEPTEMBER 3RD 2021

Numerical simulation of the transport of nanoparticles as drug carriers in hydromagnetic blood flow through a diseased artery with vessel wall permeability and rheological effects

Jayati Tripathi[1], B. Vasu[1]*, O. Anwar Bég[2] and Rama Subba Reddy Gorla[3]

[1]Department of Mathematics, Motilal Nehru National Institute of Technology Allahabad, Prayagraj, Uttar Pradesh- 211004, ***India***
[2]Department of Mechanical and Aeronautical Engineering, School of Science, Engineering and Environment (SEE), Newton Building, Salford University, Manchester, M54WT, ***UK.***
[3]Department of Aeronautics and Astronautics, Air Force Institute of Technology, Wright Patterson Air Force Base, Dayton, Ohio 45433, ***USA***
**Corresponding author- email:* bvasu@mnnit.ac.in

ABSTRACT:

The present study considers the mathematical modelling of unsteady non-Newtonian hydro-magnetic nano-hemodynamics through a rigid cylindrical artery featuring two different stenoses (composite and irregular). The Ostwald-De Waele power-law fluid model is adopted to simulate the non-Newtonian characteristics of blood. Inspired by drug delivery applications for cardiovascular treatments, blood is considered doped with a homogenous suspension of biocompatible nanoparticles. The arterial vessel exhibits the permeability effect (lateral influx/efflux), and an external magnetic field is also applied in the radial direction to the flow. A combination of the Buongiorno and Tiwari-Das nanoscale models is adopted. The strongly nonlinear nature of the governing equations requires a robust numerical method, and therefore the finite difference technique is deployed to solve the resulting equations. Validation of solutions for the pure blood case (absence of nanoparticles) is included. Comprehensive solutions are presented for shear-thickening (n=1.5) and shear-thinning (n=0.5) blood flow for the effects of crucial nanoscale thermophysical, solutal parameters, and hydrodynamic parameters. Comparison of profiles (velocity, temperature, wall shear stress, and flow rate) is also made for composite and irregular stenosis. Colour visualization of streamline plots is included for pure blood and nano mediated blood both with and without applied magnetic field. The inclusion of nanoparticles (Cu/blood) within blood increases the axial velocity of blood. By applying external magnetic field in the radial direction, axial velocity is significantly damped whereas much less dramatic alterations are computed in blood temperature and concentration profiles. The simulations are relevant to the diffusion of nano-drugs in magnetic targeted treatment of stenosed arterial diseases.

KEYWORDS: *Stenosis; non-Newtonian fluid (power-law fluid), nanofluid drug delivery, permeability, Magnetic field, finite difference method.*

NOMENCLATURE

Roman

B_1	Pressure gradient parameter
B_0	Uniform magnetic field
C	Nanoparticle concentration
d	Distance of stenosis from origin
Da	Darcy number (vessel wall permeability parameter)
D_B	Brownian diffusion coefficient
D_T	Diffusion coefficient
Gr_T	Thermal Grashof number
Gr_N	Nanoparticle Grashof number
Le	Lewis number
l_0	Length of stenosis
M	Magnetic parameter
n	Power-law rheological index
Nb	Brownian motion parameter
Nt	Thermophoresis parameter
Pr	Prandtl number
p	Pressure
Q	Flow rate
r	Radial co-ordinate
R	Radius of the artery (stenotic)
R_o	Radius of the artery (non-stenotic)
Re	Reynolds Number
S^{rr}, S^{rz}, S^{zz}	Stress tensor components
t	Time
T	Temperature
T_w	Wall temperature
u	Radial velocity
U_o	Reference velocity
w	Axial velocity
We	Weissenberg number
w_B	Slip Velocity
z	Axial co-ordinate

Greek

θ	Dimensionless temperature
σ	Dimensionless concentration
μ_0	Reference viscosity
ρ	Density
ϕ	Dimensionless nanoparticle concentration
C_p	Heat capacitance
k	Thermal conductivity

η_0	Viscosity constant
δ	Depth of stenosis
γ	Thermal expansion coefficient
τ	Wall shear stress
σ_{nf}	Nanoparticle electrical conductivity

1. INTRODUCTION:

The study of stenotic hemodynamics in arteries is a critical area of interest owing to many significant applications in cardiovascular diseases such as atherosclerosis, aneurysms, angina, or heart attacks which are among the leading causes of deaths worldwide. Cardiovascular diseases often arise in coronary arteries and are associated with the deposition of fatty substances inside the arterial wall lumen. Several studies have been carried out theoretically and experimentally to understand the exact mechanisms of stenosis development and its influence on blood flow characteristics. Shareghi and Toghraie [1] addressed the computational hemodynamics in healthy human arteries by using the finite volume method. Mishra et al. [2] studied the flow characteristics through composite stenosis while considering the arterial wall permeability effect. Srivastava et al. [3] considered the catheterized blood vessel featuring a composite stenosis. Furthermore, many fundamental studies of Newtonian blood flows have established that resistance impedance increases on increasing catheter and stenosis severity. Abdullah et al. [4] conducted a study for electrically conducting blood flow through an irregular stenosis. They presented a solution for the dimensionless time-dependent nonlinear governing equations using a robust finite difference method. From literature, it is evident that blood possesses two different characteristics, *Newtonian* and *non-Newtonian*, depending upon the shear rate conditions. Studies show that the constitutive relation of non-Newtonian models is a more accurate methodology for representing the actual characteristics of blood. Among various non-Newtonian models, the Ostwald-DeWaele power-law fluid model (and its modifications) is the most amenable approach for representing hemodynamic phenomena over different shear rates. Manica and Bortoli [5] conducted computational analysis for incompressible Newtonian and non-Newtonian blood flow through channels. In the present article, the power-law model is implemented to elucidate the shear-thinning and shear-thickening behaviour in composite stenotic arterial blood flow. Yan et al. [6] presented a numerical study of non-Newtonian (Sisko model) blood flow through an artery having a cone-shaped stenosis, giving results for different stenosis angles and Sisko parameters. Zaman

et al. [7] analyzed the blood flow numerically through a tapered catheterized artery. They assumed blood to be a non-Newtonian micropolar fluid and the artery to feature a combination of an aneurysm and stenosis. Some of the other studies considering non-Newtonian blood flow models are Toghraie et al. [8], Yan et al. [9], Foong et al. [10], Karimipour et al. [11] etc.

In recent decades, nanofluids have emerged as a significant development in biomedical engineering. Choi [12] proposed the term "nanofluid," which constitutes a suspension of different nanoparticles in a base fluid to elevate overall thermal characteristics [13-15]. The nanoparticles are usually oxides, carbides, or metals with high thermal conductivities. The base fluids include water, oil, plasma etc. Many nanoparticles are biocompatible and therefore offer almost limitless possibilities in 21st-century medical engineering. Among numerous nanotechnology applications, drug carriers allow researchers to make an effort at a molecular level to bring significant improvement in healthcare. Tripathi et al. [16] presented a detailed review of the recent blood flow advancements for nano-drug delivery systems. Vasu et al. [17] conducted a detailed finite element analysis of non-Newtonian blood flow in a stenosed coronary artery using FREEFEM++ software. Bashaga and Shaw [18] addressed a nanoparticle dispersion during nanodrug delivery in blood flow through a micro-vessel. A two-phase fluid model (non-Newtonian Herschel Bulkley model and Newtonian) is considered to define the blood characteristics. Similarly, other studies related to nanoparticle drug delivery are presented by Roy and Shaw [19], Maiti et al. [20], Shaw [21] and Tripathi et al. [22].

An important feature of real arteries is the *permeability of the blood vessel*. This property permits the diffusion of oxygen and other key nutrients through the vessel into the streaming blood flow. Many computational investigations have been communicated in recent years for hemodynamic transport with the arterial wall permeability. Bali and Awasthi [23] presented a detailed study for hemodynamic flow through a composite artery with a porous wall also considering Newtonian blood flow characteristics. Likewise, further studies addressing the effects of permeability or various stenoses have been communicated by Singh *et al*. [24], Tripathi [25], and Eldesoky [26]. The presence of iron in the hemoglobin molecule (established by Nobel Laurate, L. Pauling at Caltech in the 1930s) and the frequent presence of ions in the blood render it electrically conducting. Applying *a static or alternating* magnetic field therefore produces magnetohydrodynamic behaviour in streaming blood. This property of blood can be exploited in

bio-magnetic therapy to treat arterial diseases like atherosclerosis [27]. In different cardiac operations, magnetic blood pumps etc, extra-corporeal magnetic fields can be deployed to control surgical circuits to invoke MHD behaviour to regulate the blood volumetric flow rate. Ali et al. [28] analyzed the transient hydromagnetic blood flow, heat, and mass transfer model with nano-doping and the Buongiorno nanoscale model in a tapered stenotic artery. Haik *et al.* [29] noted that on applying the magnetic field of 10 Tesla intensity, a reduction of 30% in blood flow volume rate is achievable. A similar reduction has also been produced by Yadav *et al.* [30] but with a magnetic field of much smaller magnitude (0.002 Tesla) in the stenotic area. Nadeem *et al.* [31] studied magnetohydrodynamic blood flow in a stenosed artery, also noting that stronger transverse static magnetic field reduces the blood flow velocity in that area.

With the motivation of these above-mentioned studies, in the current investigation, a novel mathematical model is developed for *time-dependent nano-magnetohydrodynamic (Cu/blood) diseased arterial hemodynamics considering two different stenosis (composite and irregular*). To represent the non-Newtonian characteristics of blood, the power-law fluid model is applied. An external static radial magnetic field is included, although magnetic induction effects are neglected (small magnetic Reynolds number approximation). In addition, the permeability of blood vessel and pulsatile pressure gradient effects are implemented to provide a more realistic representation of actual blood flows. Heat generation effects are also included in the energy balance. The Buongiorno nanoscale model takes into account the Brownian motion and thermophoresis effect in energy equation and found that absolute velocity of nanofluid which could be estimated as sum of base fluid velocity to relative velocity. On the other hand, the Tiwari-Das nanofluid model examined nanofluid behaviour by considering the solid volume fraction. Considering the all factors, a combination of the Buongiorno and Tiwari-Das nanoscale model is adopted allowing Brownian motion, thermophoresis, nano-particle diffusion and different nanoparticles to be studied simultaneously. The main novelty of this research is therefore the *combination of nanoparticles (Cu) with applied external magnetic field, considering non-Newtonian characteristics of blood as a power-law fluid, vessel permeability and both nanoparticle species diffusion and nanoparticle types*. These characteristics have to the authors' knowledge not been considered *simultaneously* thus far in a single model in biomedical applications. The normalized (non-dimensional) non-linear conservation equations are solved by efficient finite difference method (FTCS). Further simulations and visualizations are produced in MATLAB software. The

remainder of the article is divided into the following sections: Section 2 illustrates the arterial geometry of model (for composite and irregular stenosis) with associated geometric formulations. Section 3 explains the mathematical formulation based on the nanofluid model and elaborates on the partial differential conservation equations (mass, momentum, energy and nanoparticle species) and boundary conditions. In section 4, non-dimensionalization of the boundary value problem is performed, which permits the introduction of key scaling parameters i.e., Reynolds number, Lewis number, Brownian dynamics parameter, magnetic body force parameter etc. Section 5 provides a detailed explanation of FTCS numerical technique. Section 6 presents a comprehensive validation of problem. Section 7 contains all the results and physical discourse for the impact of selected parameters on velocity, temperature, nanoparticle concentration (volume fraction), wall shear stress, flow rate and resistance impedance profile. Lastly, in section 8, the principal findings of the study are summarized with some pathways suggested for future work in nano-hemodynamics.

2. GEOMETRY OF THE MODEL:

In this study, a bi-directional rheological blood flow model for transport in the human coronary artery is taken into account, wherein the blood (base fluid) is doped with nanoparticles i. e. *nanomediated*. Blood characteristics are simulated with Ostwald-DeWaele power-law fluid model. Unsteady, incompressible, laminar flow is considered through an axisymmetric (rigid cylindrical but porous walled) artery as a representation of a diseased segment featuring two different stenoses; one is a *composite stenosis* while the other is an *irregular stenosis*. Owing to the unsteady nature of the blood flow, pulsatile pressure gradient effects in streaming blood are considered. The mathematical equations representing both geometrical configurations of the stenosed artery [32] are formulated in a cylindrical coordinate system (r,θ,z) as:

(i) *Composite Stenosis*:

$$R(z,t)=\begin{cases} R_0-2\delta(z-2d), & d\le z\le d+l_o \\ R_0-\left(\frac{\delta}{2}\right)\left(1+\cos 2\pi\left(z-2d-\left(\frac{l_o}{2}\right)\right)\right)', & d+l_o\le z\le 2l_o \\ R_0, & otherwise \end{cases} \tag{1}$$

(ii) *Irregular symmetric stenosis*:

$$R(z,t)=\begin{Bmatrix} R_0-2\delta\left(\begin{matrix}\cos\left(2\pi\left(\frac{z-d}{2}-\frac{l_0}{4}\right)\right)-\\ \left(\frac{7}{100}\right)\left(\cos\left(32\pi\left(z-2d-\left(\frac{l_o}{2}\right)\right)\right)\right)\end{matrix}\right), & d\le z\le d+l_o \\ R_0, & otherwise \end{Bmatrix} \quad (2)$$

Since the flow is taken as axisymmetric, hence the contribution of the azimuthal i. e. tangential (circumferential) (θ) direction is neglected. In the above expressions, $R(z)$ is the radius of stenotic artery, R_0 denotes the radius of non-diseased artery, δ denotes the height of stenosis, l_0 is the total length of stenosis and d is the distance of the stenosis segment from the origin (entry point to the hemodynamic flow regime). Figure 1(a) and (b) shows the geometry of the artery with both different stenosis.

3. MATHEMATICAL BIO-RHEOLOGICAL NANO-HEMODYNAMIC TRANSPORT MODEL:

Considering that the blood flowing through the artery is unsteady and bi-directional, the velocity, temperature and nano-particle concentration fields can be presented as:

$$\vec{V}=[u(r,z,t),0,w(r,z,t)]$$

$$T=T(r,z,t)$$

$$C=C(r,z,t) \quad (3)$$

In equation (3), the radial and the axial velocity components are denoted by u and w respectively. Therefore, the conservation equations for mass, momentum, energy and nanoparticle concentration (volume fraction) for the nano-mediated stenotic blood flow can be expressed as follows [33]:

$$\frac{\partial u}{\partial r}+\frac{u}{r}+\frac{\partial w}{\partial z}=0 \quad (4)$$

$$\rho_{nf}\left[\frac{\partial w}{\partial t}+u\frac{\partial w}{\partial r}+w\frac{\partial w}{\partial z}\right]=-\frac{\partial p}{\partial z}+\mu_{nf}\left[\frac{1}{r}\frac{\partial}{\partial r}\left(rS^{rz}\right)+\frac{\partial}{\partial z}\left(S^{zz}\right)\right]+ \quad (5)$$
$$\left(\rho\gamma\right)_{nf}g\left(T-T_1\right)+\left(\rho\gamma\right)_{nf}g\left(C-C_1\right)-\sigma_{nf}B_0^2w$$

$$\rho_{nf}\left[\frac{\partial u}{\partial t}+u\frac{\partial u}{\partial r}+w\frac{\partial u}{\partial z}\right]=-\frac{\partial p}{\partial r}+\mu_{nf}\left[\frac{1}{r}\frac{\partial}{\partial r}\left(rS^{rr}\right)+\frac{\partial}{\partial z}\left(S^{rz}\right)\right] \tag{6}$$

$$(\rho C_P)_{nf}\left[\frac{\partial T}{\partial t}+u\frac{\partial T}{\partial r}+w\frac{\partial T}{\partial z}\right]=k_{nf}\left[\frac{\partial^2 T}{\partial r^2}+\frac{1}{r}\frac{\partial T}{\partial r}+\frac{\partial^2 T}{\partial z^2}\right]+$$
$$\frac{(\rho C_P)_S}{(\rho C_P)_f}\left[D_B\left(\frac{\partial C}{\partial r}\frac{\partial T}{\partial r}+\frac{\partial C}{\partial z}\frac{\partial T}{\partial z}\right)+\frac{D_T}{(T_w-T_1)}\left(\left(\frac{\partial T}{\partial r}\right)^2+\left(\frac{\partial T}{\partial z}\right)^2\right)\right] \tag{7}$$

$$\left[\frac{\partial C}{\partial t}+u\frac{\partial C}{\partial r}+w\frac{\partial C}{\partial z}\right]=D_B\left[\frac{\partial^2 C}{\partial r^2}+\frac{1}{r}\frac{\partial C}{\partial r}+\frac{\partial^2 C}{\partial z^2}\right]+\frac{D_T}{(T_w-T_1)}\left[\frac{\partial^2 T}{\partial r^2}+\frac{1}{r}\frac{\partial T}{\partial r}+\frac{\partial^2 T}{\partial z^2}\right] \tag{8}$$

(8)

In equation (5), the last term i. e. the Lorentzian drag force term is due to the applied magnetic field in electrically conducting blood flow. Ohm's law explains the relationship between electrical and magnetic fields, and for low Reynolds numbers, can be written as [49]:

$$\vec{J}\mathrm{X}\vec{B}'=-\sigma_{nf}B_0{}^2\vec{V} \tag{9}$$

The physical parameters that emerge in the above set of equations are defined as follows: ρ_{nf} is the density, μ_{nf} is the viscosity, γ_{nf} is the thermal expansion coefficient, σ_{nf} is electrical conductivity, k_{nf} is thermal conductivity and $(C_p)_{nf}$ is the specific heat at constant pressure for nanofluid model, D_B shows the Brownian diffusion coefficient, T_1 is reference temperature, T_w is arterial wall temperature and D_T is the diffusion coefficient. B_0 presents the uniform magnetic field. The Cauchy stress tensor for a power law fluid is given by [49]:

$$\vec{T}=-pI+\mu\Pi^{n-1}\vec{A_1}\,, \tag{10}$$

Here *p* represents the pressure, I is the identity tensor, *n* is the rheological power-law index (*n*< 1 for pseudoplastic blood, *n* = 1 for Newtonian blood and *n* > 1 for dilatant blood), A_1 is the first Rivilin- Ericksen tensor, where [49]

$$\vec{A_1}=\vec{L}+\vec{L}^T\,, \tag{11}$$

$$L = \nabla u\,, \tag{12}$$

And
$$\Pi = \sqrt{\frac{1}{2} trace(\vec{A}_1^2)} \tag{13}$$

Extra stress tensor components $\left(S^{rr}, S^{zz}, S^{rz}\right)$ in the power-law fluid model [34] take the following form:

$$S^{zz} = -2m\left(\frac{\partial w}{\partial z}\right) \tag{14}$$

$$S^{rr} = -2m\left(\frac{\partial u}{\partial r}\right) \tag{15}$$

$$S^{rz} = -m\left(\frac{\partial w}{\partial r} + \frac{\partial u}{\partial z}\right) \tag{16}$$

Where
$$m = \left\{ \left| \left[2\left(\frac{\partial u}{\partial r}\right)^2 + 2\left(\frac{u}{r}\right)^2 + 2\left(\frac{\partial w}{\partial z}\right)^2 + \left(\frac{\partial u}{\partial z} + \frac{\partial w}{\partial r}\right)^2 \right]^{1/2} \right|^{(n-1)} \right\} \tag{17}$$

4. NON-DIMENSIONALIZATION OF NANO-HEMODYNAMIC TRANSPORT MODEL:

The mathematical model defined by Equations (4-8) can be made dimensionless with the help of the following set of scaling parameters [33]:

$$\bar{r} = \frac{r}{R_0},\ \bar{w} = \frac{w}{U_0},\ \bar{t} = \frac{U_0 t}{R_0},\ \bar{z} = \frac{z}{l_0},\ \bar{R} = \frac{R}{R_0},\ \bar{u} = \frac{l_0 u}{\delta^* U_0},\ \bar{p} = \frac{R_0^2 p}{U_0 l_0 \mu_f},\ N_b = \frac{\tau D_B C_1}{k_f},$$

$$\tau = \frac{(\rho C_p)_S}{(\rho C_p)_f},\ \bar{S}^{zz} = \frac{l_0}{U_0 \mu_f} S^{zz},\ \bar{S}^{rr} = \frac{l_0}{U_0 \mu_f} S^{rr},\ \bar{S}^{rz} = \frac{R_0}{U_0 \mu_f} S^{rz},\ \theta = \frac{T - T_1}{T_w - T_1}$$

$$Gr_N = \frac{\rho_f g R_0^2 \gamma C_1}{\mu_f U_0},\ Gr_T = \frac{\rho_f g R_0^2 \gamma (T_w - T_1)}{\mu_f U_0},\ \sigma = \frac{C - C_1}{C_1},\ \mathrm{Re} = \frac{\rho_f U_0 R_0}{\mu_f},\ L\mathrm{e} = \frac{\mu_f}{\rho_f D_B},$$

$$M = \sqrt{\frac{\sigma_f}{\mu_f}} B_0 R_0,\ \mathrm{Pr} = \frac{(C_p)_f \mu_f}{k_f},\ N_t = \frac{\tau D_T}{k_f} \tag{18}$$

Here $\bar{r}$ presents the dimensionless radial coordinate, $\bar{w}$ is the dimensionless axial velocity, $\bar{R}$ is dimensionless radius, $\bar{z}$ is dimensionless axial coordinate, $\bar{v}$ is dimensionless radial velocity

component, $\bar{t}$ is dimensionless time, $\bar{p}$ is dimensionless pressure, θ is dimensionless blood temperature, σ is the dimensionless concentration profile. U_o appears as a reference velocity of blood flow and T_w is wall temperature. μ_f is blood viscosity, $\bar{S}^{rr}$, $\bar{S}^{rz}$, $\bar{S}^{zz}$ are the dimensionless extra shear stress components. In addition to this, Pr is the Prandtl number, Re is the Reynolds number, Gr_N is the Grashof number, Gr_T is the thermal Grashof number, Le is the Lewis number, Nb is Brownian motion parameter, Nt is the thermophoresis parameter and M is the magnetic interaction (Hartmann number) parameter. In the above-defined variables, the non-dimensional geometric parameters are stenosis height parameter $\left(\delta = \delta^*/R_0\right)$ and vessel aspect ratio $(\varepsilon = R_0/l_o)$. Introducing the above-defined variables given in Eqn. (18) and after dropping the bars, equations (4)-(8) will take the form:

$$\delta\left[\frac{\partial u}{\partial r}+\frac{u}{r}\right]+\frac{\partial w}{\partial z}=0 \tag{19}$$

$$\left(\frac{\rho_{nf}}{\rho_f}\right)\mathrm{Re}\left[\frac{\partial w}{\partial t}+(\delta\varepsilon)u\frac{\partial w}{\partial r}+(\varepsilon)w\frac{\partial w}{\partial z}\right]=-\left(\frac{\partial p}{\partial z}\right)+\mu_{nf}\left[\frac{1}{r}\frac{\partial}{\partial r}\left(rS^{rz}\right)+\varepsilon^2\frac{\partial}{\partial z}(S^{zz})\right] +\frac{(\rho\gamma)_{nf}}{(\rho\gamma)_f}Gr_T\theta+\frac{(\rho\gamma)_{nf}}{(\rho\gamma)_f}Gr_N\sigma-\left(\frac{\sigma_{nf}}{\sigma_f}\right)M^2w \tag{20}$$

$$\rho_{nf}\left(\frac{\delta U_0R_0^3}{l_0^2\mu_f}\right)\left[\frac{\partial u}{\partial t}+(\delta\varepsilon)u\frac{\partial u}{\partial r}+(\varepsilon)w\frac{\partial u}{\partial z}\right]=-\left(\frac{\partial p}{\partial r}\right)+\mu_{nf}\varepsilon^2\left[\frac{1}{r}\frac{\partial}{\partial r}\left(rS^{rr}\right)+\frac{\partial}{\partial z}(S^{rz})\right] \tag{21}$$

$$\left(\frac{(\rho C_p)_{nf}}{(\rho C_p)_f}\right)\mathrm{Re}\,\mathrm{Pr}\left[\frac{\partial\theta}{\partial t}+(\delta\varepsilon)u\frac{\partial\theta}{\partial r}+(\varepsilon)w\frac{\partial\theta}{\partial z}\right]=\left(\frac{k_{nf}}{k_f}\right)\left[\frac{\partial^2\theta}{\partial r^2}+\frac{1}{r}\frac{\partial\theta}{\partial r}+\varepsilon^2\frac{\partial^2\theta}{\partial z^2}\right] +N_b\left[\left(\frac{\partial\sigma}{\partial r}\right)\left(\frac{\partial\theta}{\partial r}\right)+\varepsilon^2\left(\frac{\partial\sigma}{\partial z}\right)\left(\frac{\partial\theta}{\partial z}\right)\right]+N_t\left[\left(\frac{\partial\theta}{\partial r}\right)^2+\varepsilon^2\left(\frac{\partial\theta}{\partial z}\right)^2\right] \tag{22}$$

$$\mathrm{Re}\,Le\left[\frac{\partial\sigma}{\partial t}+(\delta\varepsilon)u\frac{\partial\sigma}{\partial r}+(\varepsilon)w\frac{\partial\sigma}{\partial z}\right]=\left[\frac{\partial^2\sigma}{\partial r^2}+\frac{1}{r}\frac{\partial\sigma}{\partial r}+\varepsilon^2\frac{\partial^2\sigma}{\partial z^2}\right]+\frac{N_t}{N_b}\left[\frac{\partial^2\theta}{\partial r^2}+\frac{1}{r}\frac{\partial\theta}{\partial r}+\varepsilon^2\frac{\partial^2\theta}{\partial z^2}\right] \tag{23}$$

Consequently, dimensionless quantities for shear stress of non-Newtonian power-law fluid model are described as:

$$S^{zz} = -\frac{2m}{\mu_f}\left(\frac{\partial w}{\partial z}\right), \qquad S^{rr} = -2m\left(\frac{\delta}{\mu_f}\right)\left(\frac{\partial u}{\partial r}\right), \qquad S^{rz} = -m\left[\frac{1}{\mu_f}\left(\frac{\partial w}{\partial r}\right)+\left(\frac{\delta\varepsilon^2}{\mu_f}\right)\left(\frac{\partial u}{\partial z}\right)\right] \tag{24}$$

$$m = \left\{\left|\left[2\left(\frac{\delta^2 U_0^2}{l_0^2}\right)\left(\frac{\partial u}{\partial r}\right)^2 + 2\left(\frac{\delta^2 U_0^2}{l_0^2}\right)\left(\frac{u}{r}\right)^2 + 2\left(\frac{U_0^2}{l_0^2}\right)\left(\frac{\partial w}{\partial z}\right)^2 + \left(\left(\frac{\delta^* U_0}{l_0^2}\right)\left(\frac{\partial u}{\partial z}\right)+\left(\frac{U_0}{R_0}\right)\left(\frac{\partial w}{\partial r}\right)\right)^2\right]^{1/2}\right|^{(n-1)}\right\} \tag{25}$$

With regard to the ensuing analysis, two different hypotheses have been taken into account; $\delta \ll 1$and $\varepsilon = O(1)$ i. e. stenosis height parameter is greatly less than one, and the vessel aspect ratio is of comparable magnitude to unity. After imposing these suppositions, Eqns. (19)-(23) will be reduced to:

$$\frac{\partial w}{\partial z} = 0 \tag{26}$$

$$-\left(\frac{\partial p}{\partial r}\right) = 0 \tag{27}$$

$$\left(\frac{\rho_{nf}}{\rho_f}\right)\mathrm{Re}\left[\frac{\partial w}{\partial t}\right] = -\left(\frac{\partial p}{\partial z}\right) + \mu_{nf}\left[\frac{1}{r}\frac{\partial}{\partial r}\left(rS^{rz}\right)\right] + \frac{(\rho\gamma)_{nf}}{(\rho\gamma)_f}Gr_T\theta + \frac{(\rho\gamma)_{nf}}{(\rho\gamma)_f}Gr_N\sigma - \left(\frac{\sigma_{nf}}{\sigma_f}\right)M^2 w \tag{28}$$

$$\left(\frac{(\rho C_p)_{nf}}{(\rho C_p)_f}\right)\mathrm{Re}\,\mathrm{Pr}\left[\frac{\partial\theta}{\partial t}\right] = \left(\frac{k_{nf}}{k_f}\right)\left[\frac{\partial^2\theta}{\partial r^2}+\frac{1}{r}\frac{\partial\theta}{\partial r}\right] + N_b\left[\left(\frac{\partial\sigma}{\partial r}\right)\left(\frac{\partial\theta}{\partial r}\right)\right] + N_t\left[\left(\frac{\partial\theta}{\partial r}\right)^2\right] \tag{29}$$

$$\mathrm{Re}\,Le\left[\frac{\partial\sigma}{\partial t}\right] = \left[\frac{\partial^2\sigma}{\partial r^2}+\frac{1}{r}\frac{\partial\sigma}{\partial r}\right] + \frac{N_t}{N_b}\left[\frac{\partial^2\theta}{\partial r^2}+\frac{1}{r}\frac{\partial\theta}{\partial r}\right] \tag{30}$$

Similarly, applying the two hypotheses, the constant *m* and shear stress component, S^{rz} of non-Newtonian fluid are further defined as:

$$m=\left\{\left|\left[2\left(\frac{U_0^2}{l_0^2}\right)\left(\frac{\partial w}{\partial z}\right)^2+\left(\frac{U_0{}^2}{R_0{}^2}\right)\left(\frac{\partial w}{\partial r}\right)^2\right]^{1/2}\right|^{(n-1)}\right\}=\left\{\left|\left[\left(\frac{U_0^2}{R_0^2}\right)\left\{\left(\frac{\partial w}{\partial r}\right)^2+2\varepsilon^2\left(\frac{\partial w}{\partial z}\right)^2\right\}\right]^{1/2}\right|^{(n-1)}\right\}=$$

$$=\left\{\left|\left[(We)^2\left(\frac{\partial w}{\partial r}\right)^2\right]^{1/2}\right|^{(n-1)}\right\}=\left\{(We)^2\left|\frac{\partial w}{\partial r}\right|^2\right\}^{(n-1)/2} \tag{31}$$

$$S^{rz}=-\frac{1}{\mu_f}\left\{(We)^2\left|\frac{\partial w}{\partial r}\right|^2\right\}^{(n-1)/2}\left(\frac{\partial w}{\partial r}\right) \tag{32}$$

In equation (32), $We=\left(U_0/R_0\right)$ is the Weissenberg number which characterizes the relative effect of *elastic force* to *viscous force* in the non-Newtonian nano-doped blood. Further, inserting S^{rz} i.e. Eqn. (32) in Eqn. (28) the latter (momentum conservation) emerges as:

$$\left(\frac{\rho_{nf}}{\rho_f}\right)\mathrm{Re}\left[\frac{\partial w}{\partial t}\right]=-\left(\frac{\partial p}{\partial z}\right)-\left(\frac{\mu_{nf}}{\mu_f}\right)\left[\frac{1}{r}\frac{\partial}{\partial r}\left\{r\left[\left\{(We)^2\left|\frac{\partial w}{\partial r}\right|^2\right\}^{(n-1)/2}\left(\frac{\partial w}{\partial r}\right)\right]\right\}\right]+\frac{(\rho\gamma)_{nf}}{(\rho\gamma)_f}Gr_T\theta+$$
$$\frac{(\rho\gamma)_{nf}}{(\rho\gamma)_f}Gr_N\sigma-\left(\frac{\sigma_{nf}}{\sigma_f}\right)M^2w \tag{33}$$

Additionally, the *non-dimensional* form for the geometric relations represented by Eqns. (1) and (2) is given as:

(i) *Composite Stenosis*-

$$R(z)=\begin{cases}1-2\delta(z-2d), & d\le z\le d+1\\ 1-\left(\frac{\delta}{2}\right)\left(1+\cos 2\pi\left(z-2d-\left(\frac{1}{2}\right)\right)\right)', & d+1\le z\le 2\\ 1, & otherwise\end{cases} \tag{34}$$

(ii) *Irregular Stenosis*-

$$R(z,t)=\begin{cases}1-2\delta\left(\begin{array}{l}\cos\left(2\pi\left(\frac{z-d}{2}-\frac{1}{4}\right)\right)-\\ \left(\frac{7}{100}\right)\left(\cos\left(32\pi\left(z-2d-\left(\frac{1}{2}\right)\right)\right)\right)\end{array}\right), & d\le z\le d+1\\ 1, & otherwise\end{cases} \tag{35}$$

The equations for the thermophysical properties of nanofluid (i.e. blood doped with nanoparticles) are defined following [35]:

$$\mu_{nf} = \frac{\mu_f}{(1-\phi)^{5/2}}, \qquad \rho_{nf} = (1-\phi)\rho_f + \phi\rho_s$$

$$(\rho C_p)_{nf} = (1-\phi)(\rho C_p)_f + \phi(\rho C_p)_s, \qquad (\rho\gamma)_{nf} = (1-\phi)(\rho\gamma)_f + \phi(\rho\gamma)_s$$

$$\frac{\sigma_{nf}}{\sigma_f} = \frac{\sigma_s + 2\sigma_f - 2\phi(\sigma_f - \sigma_s)}{\sigma_s + 2\sigma_f + \phi(\sigma_f - \sigma_s)}, \qquad \frac{k_{nf}}{k_f} = \frac{k_s + 2k_f - 2\phi(k_f - k_s)}{k_s + 2k_f + \phi(k_f - k_s)} \tag{36}$$

In the above-mentioned equations, μ_f is the viscosity of the base fluid, ρ_f as density, $(\rho C_p)_f$ is heat capacitance, γ_f is thermal expansion coefficient, σ_f is electrical conductivity and k_f is the thermal conductivity of the base fluid. For two different nanoparticles (i.e. hybrid nanofluids), (ϕ_1, ϕ_2) stands for the volume fraction, (ρ_{S_1}, ρ_{S_2}) is the density of solid particles, $[(\rho C_p)_{S_1}, (\rho C_p)_{S_2}]$ is the heat capacitance, $[\gamma_{S_1}, \gamma_{S_2}]$ is a thermal expansion coefficient, $[\sigma_{S_1}, \sigma_{S_2}]$ is electrical conductivity, and $[k_{S_1}, k_{S_2}]$ is thermal conductivity of solid nanoparticles, respectively. Introducing the nanofluid properties in Eqns. (33), (29) and (30), the emerging conservation equations take the form:

$$\left[(1-\phi) + \phi\left(\frac{\rho_s}{\rho_f}\right)\right]\mathrm{Re}\left[\frac{\partial w}{\partial t}\right] = -\left(\frac{\partial p}{\partial z}\right) - \left(\frac{1}{(1-\phi)^{5/2}}\right)\left[\frac{1}{r}\frac{\partial}{\partial r}\left\{r\left[\left\{(We)^2\left|\frac{\partial w}{\partial r}\right|^2\right\}^{(n-1)/2}\left(\frac{\partial w}{\partial r}\right)\right]\right\}\right] + \left[(1-\phi) + \phi\left(\frac{(\rho\gamma)_s}{(\rho\gamma)_f}\right)\right]Gr_T\theta + \left[(1-\phi) + \phi\left(\frac{(\rho\gamma)_s}{(\rho\gamma)_f}\right)\right]Gr_N\sigma - \left(\frac{\sigma_s + 2\sigma_f - 2\phi(\sigma_f - \sigma_s)}{\sigma_s + 2\sigma_f + \phi(\sigma_f - \sigma_s)}\right)M^2 w \tag{37}$$

$$\left[(1-\phi) + \phi\left(\frac{(\rho C_p)_s}{(\rho C_p)_f}\right)\right]\mathrm{Re}\,\mathrm{Pr}\left[\frac{\partial\theta}{\partial t}\right] = \left(\frac{k_s + 2k_f - 2\phi(k_f - k_s)}{k_s + 2k_f + \phi(k_f - k_s)}\right)\left[\frac{\partial^2\theta}{\partial r^2} + \frac{1}{r}\frac{\partial\theta}{\partial r}\right] + N_b\left[\left(\frac{\partial\sigma}{\partial r}\right)\left(\frac{\partial\theta}{\partial r}\right)\right] + N_t\left[\left(\frac{\partial\theta}{\partial r}\right)^2\right] \tag{38}$$

$$\mathrm{Re}\,Le\left[\frac{\partial\sigma}{\partial t}\right] = \left[\frac{\partial^2\sigma}{\partial r^2} + \frac{1}{r}\frac{\partial\sigma}{\partial r}\right] + \frac{N_t}{N_b}\left[\frac{\partial^2\theta}{\partial r^2} + \frac{1}{r}\frac{\partial\theta}{\partial r}\right] \tag{39}$$

Subsequently, with the help of Burton [36], the *axial pressure gradient* can be represented as:

$$-\frac{\partial p}{\partial z} = A_o + A_1 \cos(2\pi w_p)t, \quad t > 0 \tag{40}$$

Here A_0 is the *mean pressure gradient* and A_1 designates the amplitude of the pulsatile component, which is subjected to *diastolic and systolic pressures*. By using non-dimensional parameters, the normalized form of Eqn. (40) becomes:

$$-\frac{\partial p}{\partial z} = B_1[1 + e\cos(c_1 t)] \tag{41}$$

$$\text{Where } e = \frac{A_1}{A_o}, \qquad B_1 = \frac{A_o {R_0}^2}{\mu_f U_o}, \quad c_1 = \frac{2\pi R_0 w_p}{U_o} \tag{42}$$

Invoking Eqn. (41) into the given *axial momentum* equation, Eq. (37) then becomes:

$$\left[(1-\phi) + \phi\left(\frac{\rho_s}{\rho_f}\right)\right]\mathrm{Re}\left[\frac{\partial w}{\partial t}\right] = B_1\left[1 + e\cos(c_1 t)\right] - \left(\frac{1}{(1-\phi)^{5/2}}\right)\left[\frac{1}{r}\frac{\partial}{\partial r}\left\{r\left[\left\{(We)^2\left|\frac{\partial w}{\partial r}\right|^2\right\}^{(n-1)/2}\left(\frac{\partial w}{\partial r}\right)\right]\right\}\right] + \left[(1-\phi) + \phi\left(\frac{(\rho\gamma)_s}{(\rho\gamma)_f}\right)\right]Gr_T\theta + \left[(1-\phi) + \phi\left(\frac{(\rho\gamma)_s}{(\rho\gamma)_f}\right)\right]Gr_N\sigma - \left(\frac{\sigma_s + 2\sigma_f - 2\phi(\sigma_f - \sigma_s)}{\sigma_s + 2\sigma_f + \phi(\sigma_f - \sigma_s)}\right)M^2 w \tag{43}$$

Further, Eqns. (43), (38) and (39) are subject to the following boundary and initial conditions:

$$w(r,t)\big|_{r=R} = w_B, \qquad \theta(r,t)\big|_{r=R} = 0, \qquad \sigma(r,t)\big|_{r=R} = 0 \tag{44}$$

$$w(r,t)\big|_{r=0} = 0, \qquad \theta(r,t)\big|_{r=0} = 0, \qquad \sigma(r,t)\big|_{r=0} = 0 \tag{45}$$

$$w(r,0) = 0, \qquad \theta(r,0) = 0, \qquad \sigma(r,0) = 0 \tag{46}$$

$$\frac{\partial w}{\partial r} = \frac{\alpha}{\sqrt{Da}}\left[w_B - w_{porous}\right] \tag{47}$$

In the boundary equation (46), *Da* presents the Darcy number (a dimensionless permeability parameter characterizing the porous nature of the vessel wall), α is defined as dimensionless slip parameter, w_B is the slip velocity and w_{porous} as the velocity of permeable boundary [50]. According to Darcy's law, w_{porous} is given by: $w_{porous} = -Da\left(\frac{dP}{dz}\right)$ (48)

The hemodynamic quantities of interest are *volumetric flow rate, wall shear stress (WSS) and resistance impedance* which may be formulated as:

$$Q_1 = 2\pi \int_0^R wrdr, \tag{49}$$

$$\tau_S = -\left(\frac{\partial w}{\partial r}\right)_{r=R}, \tag{50}$$

$$\lambda = \frac{L\left(\frac{\partial p}{\partial z}\right)}{Q}. \tag{51}$$

For restraining the geometric effects, the radial coordinate transformation $x = \frac{r}{R(z)}$ is employed in the above governing equations. Hence Eqns. (43), (38), (39) and (44)-(47) are contracted to the following form:

$$\left[(1-\phi)+\phi\left(\frac{\rho_s}{\rho_f}\right)\right]\mathrm{Re}\left[\frac{\partial w}{\partial t}\right] = B_1\left[1+e\cos(c_1 t)\right] - \left(\frac{1}{(1-\phi)^{5/2}}\right)\left[\frac{1}{x}\frac{\partial}{\partial x}\left\{x\left[\left\{\left(\frac{We}{R}\right)^2\left|\frac{\partial w}{\partial x}\right|^2\right\}^{(n-1)/2}\left(\frac{\partial w}{\partial x}\right)\right]\right\}\right] + \left[(1-\phi)+\phi\left(\frac{(\rho\gamma)_s}{(\rho\gamma)_f}\right)\right]Gr_T\theta + \left[(1-\phi)+\phi\left(\frac{(\rho\gamma)_s}{(\rho\gamma)_f}\right)\right]Gr_N\sigma - \left(\frac{\sigma_s + 2\sigma_f - 2\phi(\sigma_f-\sigma_s)}{\sigma_s + 2\sigma_f + \phi(\sigma_f-\sigma_s)}\right)M^2 w \tag{52}$$

$$\left[(1-\phi)+\phi\left(\frac{(\rho C_p)_s}{(\rho C_p)_f}\right)\right]\mathrm{Re}\,\mathrm{Pr}\left[\frac{\partial\theta}{\partial t}\right] = \left(\frac{k_s + 2k_f - 2\phi(k_f-k_s)}{k_s + 2k_f + \phi(k_f-k_s)}\right)\left(\frac{1}{R^2}\right)\left[\frac{\partial^2\theta}{\partial x^2} + \frac{1}{x}\frac{\partial\theta}{\partial x}\right] + N_b\left(\frac{1}{R^2}\right)\left[\left(\frac{\partial\sigma}{\partial x}\right)\left(\frac{\partial\theta}{\partial x}\right)\right] + N_t\left(\frac{1}{R^2}\right)\left[\left(\frac{\partial\theta}{\partial x}\right)^2\right] \tag{53}$$

$$\mathrm{Re}\,Le\left[\frac{\partial\sigma}{\partial t}\right] = \left(\frac{1}{R^2}\right)\left[\frac{\partial^2\sigma}{\partial x^2} + \frac{1}{x}\frac{\partial\sigma}{\partial x}\right] + \frac{N_t}{N_b}\left(\frac{1}{R^2}\right)\left[\frac{\partial^2\theta}{\partial x^2} + \frac{1}{x}\frac{\partial\theta}{\partial x}\right] \tag{54}$$

Furthermore, the associated dimensionless boundary and initial conditions are written as:

$$w(x,t)\big|_{x=1} = w_B, \qquad \theta(x,t)\big|_{x=1} = 0, \qquad \sigma(x,t)\big|_{x=1} = 0 \tag{55}$$

$$w(x,t)\big|_{x=0}=0, \qquad \theta(x,t)\big|_{x=0}=0, \qquad \sigma(x,t)\big|_{x=0}=0 \tag{56}$$

$$\frac{\partial w}{\partial x}=\frac{\alpha R}{\sqrt{Da}}\left[w_B-w_{porous}\right], \text{ where } w_{porous}=-Da\left(\frac{dP}{dz}\right) \tag{57}$$

$$w(x,0)=0, \qquad \theta(x,0)=0, \qquad \sigma(x,0)=0 \tag{58}$$

Similarly, the *volumetric flow rate, wall shear stress (WSS) and resistance impedance* respectively [Equations (49)-(51)] take the following form:

$$Q_1=2\pi R^2\left(\int_0^1 wxdx\right), \tag{59}$$

$$\tau_S=-\frac{1}{R}\left(\frac{\partial w}{\partial x}\right)_{x=1}, \tag{60}$$

$$\lambda=\frac{L\left(\frac{\partial p}{\partial z}\right)}{Q}. \tag{61}$$

Replacing the pressure gradient term in Eqn. (61), it can be written as follows:

$$\lambda=\frac{L\left[B_1(1+e\cos(2\pi t))\right]}{2\pi R^2\left(\int_0^1 wxdx\right)}. \tag{62}$$

5. NUMERICAL SOLUTION:

To obtain the exact solution of the nonlinear partial differential equations (PDEs) describing the nano-hemodynamic stenotic magnetohydrodynamic flow regime is difficult, if not impossible. Hence it is necessary to use numerical methods for solving Eqns. (52) - (54) under the prescribed boundary and initial conditions (55)-(58). A suitable numerical technique in this regard, based on the discretization of PDEs is the explicit finite-difference FTCS (forward in time (FT) and central in space (CS) technique), which is described in Hoffmann's book [37]. Furthermore, FTCS has been verified extensively by many researchers in diverse fluid mechanical studies [38, 39] and confirmed to be very stable, rapidly convergent and easy to program. In this scheme, firstly the spatial domain is discretized and after that, the value of velocity component is calculated at each

node x_i and over the time instant t^k, which is written as w_i^k. According to Hoffmann [37] the central differencing formulation is of second order and the forward differencing formulation is of first order. The relevant partial derivatives are defined as:

$$\frac{\partial w}{\partial x} \cong \frac{w_{i+1}^k - w_{i-1}^k}{2\Delta x} = w_x, \tag{63}$$

$$\frac{\partial^2 w}{\partial x^2} \cong \frac{w_{i+1}^k - 2w_i^k + w_{i-1}^k}{(\Delta x)^2} = w_{xx}, \tag{64}$$

and $$\frac{\partial w}{\partial t} \cong \frac{w_i^{k+1} - w_i^k}{\Delta t} = w_t \tag{65}$$

Incorporating the difference equations for the partial derivatives, Eqns. (52)-(54) will readily be reduced to the following form given below:

$$w_i^{k+1} = w_i^k + \frac{\Delta t}{\mathrm{Re}\left[(1-\phi) + \phi\left(\frac{\rho_s}{\rho_f}\right)\right]}\left[\begin{array}{l} B_1\left[1 + e\cos(c_1 t^k)\right] - \left(\frac{1}{(1-\phi)^{5/2}}\right)\left[\frac{1}{x}\frac{\partial}{\partial x}\left\{x\left[\left\{\left(\frac{We}{R}\right)^2\left|\frac{\partial w}{\partial x}\right|^2\right\}^{(n-1)/2}\left(\frac{\partial w}{\partial x}\right)\right]\right\}\right] + \\ \left[(1-\phi) + \phi\left(\frac{(\rho\gamma)_s}{(\rho\gamma)_f}\right)\right]Gr_T\theta_i^k + \left[(1-\phi) + \phi\left(\frac{(\rho\gamma)_s}{(\rho\gamma)_f}\right)\right]Gr_N\sigma_i^k - \left(\frac{\sigma_s + 2\sigma_f - 2\phi(\sigma_f - \sigma_s)}{\sigma_s + 2\sigma_f + \phi(\sigma_f - \sigma_s)}\right)M^2 w_i^k \end{array}\right] \tag{66}$$

$$\theta_i^{k+1} = \theta_i^k + \frac{\Delta t}{\mathrm{Re}\,\mathrm{Pr}\left[(1-\phi) + \phi\left(\frac{(\rho C_p)_s}{(\rho C_p)_f}\right)\right]}\left[\begin{array}{l} \left(\frac{k_s + 2k_f - 2\phi(k_f - k_s)}{k_s + 2k_f + \phi(k_f - k_s)}\right)\left(\frac{1}{R^2}\right)\left[\frac{\partial^2\theta}{\partial x^2} + \frac{1}{x}\frac{\partial\theta}{\partial x}\right] + \\ N_b\left(\frac{1}{R^2}\right)\left[\left(\frac{\partial\sigma}{\partial x}\right)\left(\frac{\partial\theta}{\partial x}\right)\right] + N_t\left(\frac{1}{R^2}\right)\left[\left(\frac{\partial\theta}{\partial x}\right)^2\right] \end{array}\right] \tag{67}$$

$$\sigma_i^{k+1} = \sigma_i^k + \left(\frac{\Delta t}{\mathrm{Re}\,Le}\right)\left[\left(\frac{1}{R^2}\right)\left[\frac{\partial^2\sigma}{\partial x^2} + \frac{1}{x}\frac{\partial\sigma}{\partial x}\right] + \frac{N_t}{N_b}\left(\frac{1}{R^2}\right)\left[\frac{\partial^2\theta}{\partial x^2} + \frac{1}{x}\frac{\partial\theta}{\partial x}\right]\right] \tag{68}$$

Further, the associated boundary and initial conditions Eqns. (52)-(55) are represented by:

$$w_i^1 = \theta_i^1 = \sigma_i^1 = 0 \qquad \text{at } t = 0 \tag{69}$$

$$w_1^k = 0, \quad \theta_1^k = 0, \quad \sigma_1^k = 0 \qquad \text{at } x = 0 \tag{70}$$

$$w_{N+1}^{k} = w_B, \quad \theta_{N+1}^{k} = 0, \quad \sigma_{N+1}^{k} = 0 \quad \text{at} \quad x = 1 \tag{71}$$

$$\frac{\partial w}{\partial x} = \frac{\alpha R}{\sqrt{Da}}\left[w_B - w_{porous} \right] \tag{72}$$

In this numerical scheme, the spatial variable is discretized into *N+1* grid-points where the step size is taken as $\Delta x = 1/N+1$. The time instant is defined by t_k, where the value of t_k is given as $t_k = (k-1)\Delta t$, in which Δt denotes a small increment in time. The velocity component is further calculated at each node and for every time instant. As stability of this numerical scheme is dependent on step size and time increment, hence $\Delta x = 0.025$ and $\Delta t = 0.0001$ are prescribed in the numerical code to fulfill the stability condition. These values confirm the stability and convergence of this scheme as documented in Hoffmann's book [37]. The FTCS code has been extensively validated and implemented in numerous previous simulations including solar energy radiative heat transfer flows [40], periodic hydromagnetic flows in geophysics [41], viscoelastic blood flow with body acceleration [42], peristaltic gastro-intestinal pumping [43], thermosolutal cross fluid blood flow in tapered arteries [44] and non-Newtonian coating hydromechanics [45]. Confidence is therefore justifiably high in the FTCS scheme which is ideal for multi-physical blood flow simulations in complex geometries, as considered in the present work.

6. VALIDATION:

To validate the FTCS numerical method which has been chosen to solve the current problem, the numerical results obtained by Ijaz and Nadeem [46] (computed by using the same FTCS method) for the axial velocity profile of blood flow are compared with present results when the stenosis height (δ = 0.01) and different volume fractions (ϕ = 0.00, 0.02) over various radial coordinate values, *r* are given in **Table 2**. From the table, evidently very good correlation between the present FTCS code and the computations in [46] is achieved at all values of radial coordinate. Confidence is therefore established in the FTCS algorithm.

7. RESULTS AND DISCUSSION:

In this section, the hemodynamic characteristics of a stenosed artery in the presence of copper nanoparticles under radial magnetic field are discussed. With reference to emerging parameters,

the results for axial velocity, temperature, concentration profiles, wall shear stress, volumetric flow rate and resistance impedance are illustrated in graphical form. For computations with the FTCS code, the default values of various parameters which are used are documented in **Table 3**. These values are consistent with actual clinical scenarios and have been extracted from a number of previous studies [32-46].

Figure 2(a)-(b) exhibits the impact of nanoparticle concentration on axial blood velocity component for shear-thickening ($n>1$) and shear-thinning ($n<1$) fluids respectively. From both the figures, it can be seen that with increasing nanoparticle concentration, the velocity profile *is elevated i. e. the axial blood flow is accelerated.* It is also evident that the attained velocity magnitude is higher for shear-thickening fluid in comparison to shear-thinning fluid. Also, results are drawn for both (composite and irregular) stenosis and it is evident that velocity is comparatively less for an irregular stenosis than a composite stenosis. The addition of nanoparticle in blood is extremely favorable therefore for arterial disease blood flow manipulation as it clearly modifies the flow velocity magnitudes. **Figure 3 (a)-(b)** shows the impact of nanoparticle volume fraction on temperature and concentration profile, respectively. Temperature profile is progressively an increasing function of volume fraction while nano-particle concentration is found to be a decreasing function. The *thermal enhancement properties* of nanoparticles are therefore confirmed again with the current simulations. Additionally, for both the figures, the irregular stenosis exhibits higher maximum temperature or nano-particle concentration compared with the composite stenosis. The geometrical nature of the stenosis therefore clearly influences thermal and nano-particle diffusion in the streaming blood flow. Using only a composite stenotic model will lead to an *under-prediction* in temperature and concentration values.

Figure 4(a)-(b) depicts the influence of slip parameter (α) on velocity profiles for $n=1.5$ and $n=0.5$, respectively. In the case of shear-thickening fluid (dilatant i. e. $n > 1$), when we increase the slip parameter, then more resistance is generated to the blood flow, which results in flow retardation i.e. a depletion in velocity values. The opposite effect is generated for shear-thinning fluid i. e. $n<1$; in other words *flow acceleration* is induced since lower resistance is offered to the streaming blood. The effect of Darcy number on velocity profile is presented by Figure 5(a)-(b) for two different stenoses. For both $n=1.5$ *and* $n=0.5$, enhancement in Darcy number accelerates the blood flow indicating that greater permeability of the vessel wall adds momentum via lateral influx which

assists the streaming flow in the artery. From figures, it is seen that the irregular stenosis attains higher velocity magnitudes for shear-thickening blood while the composite stenosis achieves higher velocities for shear-thinning blood.

The velocity profiles for different Grashof numbers *Gr* are plotted in **Figure 6 (a)-(b)** for $n>1$ and $n<1$, respectively. Grashof number (Gr_T) is the ratio of thermal buoyancy force to viscous force. The species (solutal) Grashof number, Gr_N is not varied (concentration differences of nanoparticles within blood increases the species buoyancy force, although this is not plotted). Stronger thermal buoyancy effect aids in momentum development, intensifies the blood flow and is associated with a reduction in resistance to hemodynamic transport and a concomitant acceleration. Evidently flow deceleration arises with vanishing thermal buoyancy force ($Gr=0$) as seen in Figure 6 (a)-(b) and this corresponds to the purely forced convection scenario. On comparing these two figures, the maximum attained velocity is observed for shear-thickening fluid at the highest value of *Gr*.

Similarly, the effect of Lewis number (*Le*) on velocity profile is given in **Figure 7 (a)-(b)** for both types of stenosis. Lewis number is defined as the ratio of *thermal diffusivity to mass diffusivity*. The graphs show that increment in the value of *Le* manifests in a suppression in the magnitude of velocity in both the figures i. e. *flow deceleration*. For an irregular stenosis, lower velocity values are computed compared with a composite stenosis.

Figure 8 (a)- (b) depicts the evolution in velocity profile with modification in the magnetic parameter (*M*) considering the shear-thickening and shear- thinning fluid, respectively. It is apparent that a higher M value (associated with stronger Lorentzian drag force) significantly retards the blood flow around the centerline of the artery (core zone). The case of electrically non-conducting blood is retrieved for $M = 0$ i. e. vanishing radial magnetic field. For the case $M = 1$ both magnetic and viscous hydrodynamic forces are equivalent (Hartmann number, *M*, expresses the ratio of these body forces). Effectively the blood flow is regulated i. e. damped with stronger magnetic field which permits improved control of biomedical operations through a non-intrusive methodology (i. e. external magnetic field). In the shear-thickening fluid case, higher velocity is computed for an irregular stenosis while in the shear-thinning fluid, maximum velocity is associated with composite stenosis geometry, for each *M* value.

Figure 9 (a)- (b) depicts the distribution in velocity profile for different values of Brownian motion parameter (*Nb*). The *Nb* value corresponds to the nanoparticles size as high *Nb* values are representative of smaller nanoparticle and vice-versa in the adopted Buongiorno formulation. The profiles indicate that the axial velocity decreases with enhancing the parameter *Nb i. e. smaller nanoparticles result in flow deceleration*. It is also clear that in the shear-thinning case, the irregular stenosis produces lower velocities comparatively to the composite stenosis while for shear-thickening fluid, a mixed variation is seen.

The impact of thermophoresis parameter (*Nt*) on blood flow velocity is presented in **Figure 10 (a) - (b)** for both stenotic cases. Contrary to the trend induced by increment in Brownian motion parameter, the velocity profile is substantially increased with elevation in thermophoresis parameter. The thermophoretic body force (which is proportional to *Nt*) drives nanoparticles under the force of a temperature gradient. This aids in momentum development and accelerates the flow. For the shear-thickening blood case, higher velocity magnitudes are associated with the irregular stenosis whereas for shear-thinning (pseudoplastic) blood, greater velocities are obtained for the composite stenosis.

Impact of Brownian motion and thermophoresis parameter on concentration profile is presented in Figure 11 (a) - (b). From graphs, it is exhibited that on enhancing the Brownian motion parameter, the concentration is reduced while the same profile increases on increasing the thermophoresis parameter. The erratic random movement of microscopic particles in a fluid, as a result of continuous bombardment from molecules of the surrounding medium is known as Brownian motion. In nanoscale systems, this bombardment is significant, and many ballistic collisions will naturally occur. These will inhibit the overall concentration in the streaming blood flow i.e. oppose species diffusion. Additionally, for both pseudoplastic and dilatant blood flow, the irregular stenosis produces higher velocity magnitudes up to a fixed radial position whereas after this critical radius, evidently the composite stenosis attains higher velocity magnitudes up to the vessel wall.

The effect of Reynolds number (*Re*) on blood flow velocity and temperature profile is elaborated in **Figure 12 (a) - (b).** It is noteworthy that very low Reynolds numbers are considered (laminar flow) and the regime is therefore a viscous-dominated one. The graphical trends show that by increasing the value of *Re* from 1 to 5, a significant amount of reduction in velocity is produced.

In the same manner, an increment in *Re* also results in a depletion in the magnitude of temperature i. e. the streaming blood regime is cooled with greater inertial force relative to viscous force (for *Re* = 1 both forces are equivalent, and this is frequently termed "creeping flow"). Although inertial force is increased with Reynolds number, the overwhelming effect is nevertheless flow deceleration owing to the stenotic obstruction and population of nanoparticles which alter the internal dynamics of the blood flow. Figure 12 (a) also shows that a higher value of velocity is computed for shear-thickening (dilatant) blood ($n > 1$) and this progressively decreases as we move to the Newtonian ($n = 1$) and shear-thinning ($n < 1$) blood scenarios.

The impact of Weissenberg number (*We*) on blood flow velocity in the stenotic region is given in **Figure 13 (a) - (b).** It is observed that as *We* increments from 1.5 to 3.5, the velocity profile decreases for shear-thickening blood whereas it shows an enhancement for shear-thinning blood. Weissenberg number expresses the relative role of elastic and viscous forces in non-Newtonian fluid mechanics. For $We > 1$ *elastic forces dominate* and these induce deceleration in dilatant blood. The reduction in viscous forces relative to elastic forces ($We > 1$) implies a decrease in viscous resistance to the streaming blood which produces the observed acceleration in the shear-thinning (pseudoplastic) case.

The volumetric flow rate profile for various nanoparticle volume fractions through both stenotic regions considering non-Newtonian fluid (for both $n=1.5$ and $n=0.5$) is presented in **Figures 14-15**. It is clear, that, increment in volume fraction generates substantial flow rate enhancement for both cases. It is also evident that flow rate is markedly higher for the composite stenosis in comparison to the irregular stenosis. On comparing these two figures it is noted that higher flow rate is registered for $n=1.5$ i. e. the dilatant blood flow case.

Volumetric flow rate profiles for variation in the magnetic parameter (*M*) for both pseudoplastic and dilatant blood cases is displayed in **Figures 16-17**. The graphs indicate that flow rate exhibits an inverse relationship with magnetic field parameter i.e., flow rate is depressed on increasing the magnitude of magnetic field (stronger Lorentzian drag force). For both the shear-thickening and shear-thinning fluid cases, an irregular stenosis produces lower flow rate values compared to the composite stenosis. Additionally, the highest overall flow rate value is again registered for shear-thickening (dilatant) blood.

The influence of Darcy number on wall shear stress and flow rate profiles for both type of stenosis is presented in **Figures 18-21**. From figures 18-19, it can be deduced that on increasing the Darcy parameter, wall shear stress is boosted for both the blood rheology cases (*n=1.5 and n=0.5*). Again, this is due to the assistive nature of wall permeability (influx) on momentum development which accelerates the blood flow and therefore induces greater shearing effect at the wall. It is noted that in the shear-thickening blood case, an irregular stenosis attains slightly higher wall shear stress values than the composite stenosis while in the shear-thinning fluid case the contrary trend is computed i. e. the composite stenosis produces greater wall shear stresses than the irregular stenosis. Figure 20-21 illustrate the flow rate profiles for various Darcy parameters again for both shear thickening and shear thinning blood cases. On increasing the Darcy parameter from 0.05 to 0.15, accentuation in the flow rate magnitudes is produced. For both blood cases, an irregular stenosis produces comparatively lower flow rates than a composite stenosis. In shear-thinning case, negative value arises for *Da=0.05* and for this case, a wavy distribution is computed for all the parametric values.

The impact of Reynolds number on volumetric flow rate profile is presented in **Figures 22-23**. The graphs show that enhancement in the magnitude of Reynolds number results in a decrement in flow rate. In both blood rheology cases, a composite stenosis has slightly higher flow rate than an irregular stenosis and flow rate is suppressed for higher value of *Re*. On comparing these two figures, it is seen that maximum flow rate is achieved for the dilatant (shear-thickening) blood.

The effect of Weissenberg number (*We*) on wall shear stress and flow rate profile is represented in **Figures 24-27**. For both blood flow cases, an inverse trend is observed for wall shear stress as well as for flow rate profiles. In the shear-thickening case, these figures reveal that both the wall shear stress and volumetric flow rate are reduced for larger values of Weissenberg number while in the shear-thinning fluid case, both profiles are enhanced by increasing the value of Weissenberg number. Additionally, for n=1.5, in both the wall shear stress and flow rate graphs, the irregular stenosis attains slightly higher magnitudes than the composite stenosis while for n=0.5, the composite stenosis registers higher magnitudes than the irregular stenosis.

Figure 28-29 display the time profile of hemodynamic resistance (impedance) to flow at the stenosis throat for the considered set of parameter values and for different blood rheology cases (*n=1.5 and n=0.5*). The impedance profile shows opposite trend to volumetric flow rates as from

the mathematical formulation described earlier, it is clear that both the profiles are inversely related to each other. In both figures, the black line (ϕ=0.03) shows the impedance for the default set of parameters given in **Table 3**. Both the graphs present an almost identical trend for variation in the control parameters. The results reveal that the magnitude of resistance impedance is increased by raising the magnitude of Reynolds number (*Re*=5) and magnetic parameter (*M*=2) parameter while it is decreased by enhancement in the Weissenberg number (*We*=3.5). On comparing these two figures it is noteworthy that the magnitude of resistance impedance is much higher for the shear-thinning case compared to the shear-thickening fluid.

Table 4 presents the comparison for the values of volumetric flow rate with alteration in Brownian motion and thermophoresis parameters. The computations are given for both composite and irregular stenoses with both shear-thickening and shear-thinning blood. These values are registered at time *t*=1.0 and the other emerging parameters are taken as default values. The data indicates that on increasing the thermophoresis parameter from 0.1 to 0.5 i. e. with stronger thermophoretic body force, enhancement in flow rate profile is shown for both stenoses and comparing the data for *n=1.5 and n=0.5*, higher values are noticed for *n*=1.5 (shear-thickening). Additionally, flow rate values decrease with an increment in the Brownian motion parameter from 0.1 to 0.5, which is again associated with a decrement in velocity (flow deceleration).

To analyze the view of blood particles along the axial direction, the blood flow contour patterns are visualized in **Figure 30 panels (a)-(d)**. As each panel consists of four subfigures [(a)-(d)] which describes the streamlines for composite and irregular artery, firstly considering the shear-thickening fluid while the last two figures for shear-thinning fluid, and this also shows the randomness of the graphs. Panel (a) shows the blood flow pattern for the considered default set of parameters given in Table 3. To calculate the difference on changing the defined parameter, panel (b)-(d) will be compared with panel (a). Comparison between the panels exhibits the change in the movement of blood particles by particularly changing some specific parameters. Panel (b) displays the pattern for pure blood case with the other defaulted parameters. On comparing each sub-panel of panel (b) with the corresponding sub-panel of panel (a), it is clear, that, inclusion of nanoparticles in streaming blood flow *increases the axial velocity* and achieves marked acceleration in stenotic geometries. Panel (c) shows the blood flow pattern in the arterial region without magnetic field (*M*=0) with the other defaulted parameter values. On comparison with panel

(a), it is noted that *axial velocity is higher without magnetic field* for each case. Absence of Lorentzian body force generated by the radial magnetic field therefore results in flow acceleration whereas inclusion of the magnetic retarding force achieves the desired flow deceleration of interest in biomedical flow control applications. In the same manner, Panel (d) presents the flow pattern for changing the Weissenberg number (We=3.5). The comparison of panel (d) with panel (a) demonstrates that higher blood flow velocity is achieved with greater values of We which is again associated with the concomitant decrease in viscous forces relative to elastic forces in streaming rheological blood for $We > 1$.

8. CONCLUSIONS:

Inspired by nano-drug delivery technologies for the treatment of arterial diseases, this study provides a deeper understanding of *magneto-nano-hemodynamics of stenotic arteries* via computational simulations of hydromagnetic blood mediated nanoparticle transport through an artery having two different stenosis i.e., composite and irregular stenosis. An external radial magnetic field is also applied to a rigid permeable walled artery to simulate more accurately the electrically conducting blood flow characteristics in stenotic regions. To mimic the non-Newtonian characteristics of blood, the power-law fluid model is taken into account and comparison between shear-thickening blood (n=1.5) and shear-thinning blood (n=0.5) is investigated. For realistic flow situations, the unsteady component of pulsatile pressure gradient is also included. Further, to know blood characteristics (velocity, temperature, concentration, wall shear stress, flow rate and resistance impedance) in stenotic regions, the governing equations are solved with the help of finite difference method (FTCS). The key conclusions from the present numerical computations are summarized as follows:

- The inclusion of nanoparticles (Cu/blood) within blood increases the axial velocity of blood. Additionally, on increasing the nanoparticle volume fraction, temperature profile is boosted while concentration follows the reverse trend.
- On variation in slip parameter (α), axial velocity decreases in shear-thickening blood while it increases for shear-thinning blood. Likewise, enhancement in Darcy number (Da) causes blood flow acceleration for both blood rheological types.

- Enhancement in thermal buoyancy effect as simulated via Grashof number (Gr) increases the axial velocity while for higher values of Lewis number (Le), velocity magnitudes are suppressed i.e., flow retardation is induced for both stenoses.
- By applying external magnetic field in the radial direction, axial velocity is significantly damped whereas much less dramatic alterations are computed in blood temperature and concentration profiles.
- The axial velocity of blood increases with greater thermophoresis parameter (Nt) while the flow deceleration is produced with increasing Brownian motion (Nb) parameter. Minor modifications are generated by these parameters on temperature profiles.
- Concentration magnitudes are depressed with rising values of Brownian motion (Nb) while they are elevated with increment in thermophoresis parameter (Nt).
- On varying the Reynolds number (Re) from 1 to 5, deceleration in axial velocity and depletion in temperature magnitudes is registered for both shear-thickening and shear-thinning blood cases.
- Increasing the Weissenberg number (We) cause axial flow retardation in the shear-thickening blood case while it induces acceleration for the shear-thinning blood case.
- Wall shear stress and volumetric flow rate are boosted with increasing the magnitude of Darcy number (Da). Both profiles show enhancement for either composite or irregular stenoses.
- For shear-thickening and shear-thinning blood, resistance impedance is calculated for changing some parameters and it shows the opposite behaviour to that computed for volumetric flow rate.
- On comparing, the new results reported here show that blood flow characteristics (velocity, wall shear stress and flow rate) are always higher for shear-thickening blood flow ($n>1$) than shear-thinning blood ($n<1$). However, it does not show any influence on temperature and concentration profiles.
- For shear-thinning case, composite stenosis achieves slightly higher value comparing to irregular stenosis while reverse behaviour is registered for shear-thickening case in which irregular stenosis accomplish maximum value.

The present simulations have revealed some interesting insights into non-Newtonian magnetohydrodynamic nano-doped blood flow. However, a relatively simple rheological model has been implemented and the influence of *electrical fields* has been neglected. *Electrokinetic viscoelastic* blood flows [47] are also of great interest in nano-pharmacodynamics. Furthermore, Taylor dispersion is also of great relevance as are chemical reaction effects in oxygen diffusing through rheological blood [48]. Shape factor effects of the nanoparticles have also not been considered in the study. Additionally, the present study is restricted to a *single stenosis* and may be generalized in the future to examine the combination of stenoses and aneurysms with tapering effects. The potential benefits of nanoparticle drug and gene-eluting stents for the pretension and treatment of coronary re-stenosis [51] are also robust areas to explore with computational fluid dynamics. Future studies will be orientated in these directions and will be communicated imminently.

ACKNOWLEDGEMENTS

The authors are grateful to the Science and Engineering Research Board (SERB), Department of Science and Technology (DST), Government of India for undertaking the research work under the research project *File Number: ECR/2017/001053* dated 12/03/2018.

REFERENCES:

1. Shareghi, S., & Toghraie, D. (2016). Numerical simulation of blood flow in healthy arteries by use of the Sisko model. Computational Thermal Sciences: An International Journal, 8(4). https://doi.org/10.1615/ComputThermalScien.2016016738
2. Mishra, S., Siddiqui, S. U., & Medhavi, A. (2011). Blood flow through a composite stenosis in an artery with permeable wall. Int. J. Appl. Math. Appl, 6, 58-73. https://digitalcommons.pvamu.edu/aam/vol6/iss1/5
3. Srivastava VP, Vishnoi R, Mishra S, Sinha P. Blood flow through a composite stenosis in catheterized arteries. J Sci Tech 2015: 55-4.
4. Abdullah I, Amin N, Hayat T. Magnetohydrodynamic effects on blood flow through an irregular stenosis. Int J Numer Methods Fluids. 2011;67:1624-36. https://doi.org/10.1002/fld.2436
5. Manica R, De Bortoli AL. Simulation of sudden expansion flows for power-law fluids. J Non-Newton Fluid Mech 2004;121:35-40. https://doi.org/10.1016/j.jnnfm.2004.03.009
6. Yan, S. R., Zarringhalam, M., Toghraie, D., Foong, L. K., & Talebizadehsardari, P. (2020). Numerical investigation of non-Newtonian blood flow within an artery with cone shape of stenosis in various stenosis angles. Computer methods and programs in biomedicine, 192, 105434. https://doi.org/10.1016/j.cmpb.2020.105434
7. Zaman A, Ali N, Bég OA. Numerical simulation of unsteady micropolar hemodynamics in a tapered catheterized artery with a combination of stenosis and aneurysm. Med Biol Eng Comput 2016;54:1423-36. https://doi.org/10.1007/s11517-015-1415-3
8. Toghraie, D., Esfahani, N. N., Zarringhalam, M., Shirani, N., & Rostami, S. (2020). Blood flow analysis inside different arteries using non-Newtonian Sisko model for application in biomedical engineering. Computer methods and programs in biomedicine, 190, 105338. https://doi.org/10.1016/j.cmpb.2020.105338

9. Yan, S. R., Sedeh, S., Toghraie, D., Afrand, M., & Foong, L. K. (2020). Analysis and management of laminar blood flow inside a cerebral blood vessel using a finite volume software program for biomedical engineering. Computer methods and programs in biomedicine, 190, 105384. https://doi.org/10.1016/j.cmpb.2020.105384
10. Foong, L. K., Shirani, N., Toghraie, D., Zarringhalam, M., & Afrand, M. (2020). Numerical simulation of blood flow inside an artery under applying constant heat flux using Newtonian and non-Newtonian approaches for biomedical engineering. Computer methods and programs in biomedicine, 190, 105375. https://doi.org/10.1016/j.cmpb.2020.105375
11. Karimipour, A., Toghraie, D., Abdulkareem, L. A., Alizadeh, A. A., Zarringhalam, M., & Karimipour, A. (2020). Roll of stenosis severity, artery radius and blood fluid behavior on the flow velocity in the arteries: application in biomedical engineering. Medical hypotheses, 144, 109864. https://doi.org/10.1016/j.mehy.2020.109864
12. Choi SU, Eastman JA. Enhancing thermal conductivity of fluids with nanoparticles. Argonne National Lab., IL (United States); 1995.
13. Selimefendigil, F., & Chamkha, A. J. (2019). Magnetohydrodynamics mixed convection in a power law nanofluid-filled triangular cavity with an opening using Tiwari and Das' nanofluid model. Journal of Thermal Analysis and Calorimetry, 135(1), 419-436. https://doi.org/10.1007/s10973-018-7037-x
14. Selimefendigil, F., Oztop, H. F., & Chamkha, A. J. (2021). Jet Impingement Heat Transfer of Confined Single and Double Jets with Non-Newtonian Power Law Nanofluid under the Inclined Magnetic Field Effects for a Partly Curved Heated Wall. Sustainability, 13(9), 5086. https://doi.org/10.3390/su13095086
15. Li, Z., Selimefendigil, F., Sheikholeslami, M., Shafee, A., & Alghamdi, M. (2020). Hydrothermal analysis of nanoparticles transportation through a porous compound cavity utilizing two temperature model and radiation heat transfer under the effects of magnetic field. Microsystem Technologies, 26(2), 333-344. https://doi.org/10.1007/s00542-019-04504-1
16. Tripathi J, Vasu B, Dubey A, Gorla RS, Murthy PV, Bég OA, Prasad VR, Saikrishnan P. A review on recent advancements in the hemodynamics of nano-drug delivery systems. NanoSci Technol 2020;11:73-98. https://doi.org/10.1615/NanoSciTechnolIntJ.2020033448
17. Vasu B, Dubey A, Bég OA. Finite element analysis of non-Newtonian magnetohemodynamic flow conveying nanoparticles through a stenosed coronary artery. Heat Tran Asian Res 2020;49:33-66. https://doi.org/10.1002/htj.21598
18. Bashaga, G., & Shaw, S. (2021). Shear-augmented solute dispersion during drug delivery for three-layer flow through microvessel under stress jump and momentum slip-Darcy model. Applied Mathematics and Mechanics, 42(6), 901-914. https://doi.org/10.1007/s10483-021-2737-8
19. Roy, A. K., & Shaw, S. (2021). Shear augmented microvascular solute transport with a two-phase model: Application in nanoparticle assisted drug delivery. Physics of Fluids, 33(3), 031904. https://doi.org/10.1063/5.0035754
20. Maiti, S., Shaw, S., & Shit, G. C. (2020). Caputo–Fabrizio fractional order model on MHD blood flow with heat and mass transfer through a porous vessel in the presence of thermal radiation. Physica A: Statistical Mechanics and its Applications, 540, 123149. https://doi.org/10.1016/j.physa.2019.123149
21. Shaw, S. (2020). Effective shear augmented dispersion of solutes during nanoparticle assisted drug delivery in a microvessel. Fluid Dynamics Research, 52(1), 015510. https://doi.org/10.1088/1873-7005/ab6617
22. Tripathi, J., Vasu, B., & Bég, O. A. (2021). Computational simulations of hybrid mediated nano-hemodynamics (Ag-Au/Blood) through an irregular symmetric stenosis. Computers in Biology and Medicine, 130, 104213. https://doi.org/10.1016/j.compbiomed.2021.104213
23. Bali R, Awasthi U. Mathematical model of blood flow in small blood vessel in the presence of magnetic field. Appl Math 2011;2:264-9. https://doi.org/10.4236/am.2011.22031
24. Singh R, Sharma G C, Jain M. Mathematical modeling of blood flow in a stenosed artery under mhd effect through porous medium. Int J Eng Trans B: Appl, 2010: 23, 243-52. https://iranjournals.nlai.ir/handle/123456789/336195
25. Tripathi D. A mathematical model for blood flow through inclined arteries under the influence of inclined magnetic field. J Mech Med Biol 2012;12:1250033. https://doi.org/10.1142/S0219519411004812
26. Eldesoky IM. Slip effects on the unsteady MHD pulsatile blood flow through porous medium in an artery under the effect of body acceleration. Int J Math Math Sci 2012:860239. https://doi.org/10.1155/2012/860239
27. Tripathi, J., Vasu, B., Bég, O. A., & Gorla, R. S. R. (2021). Unsteady hybrid nanoparticle-mediated magneto-hemodynamics and heat transfer through an overlapped stenotic artery: Biomedical drug delivery simulation. Proceedings of the Institution of Mechanical Engineers, Part H: Journal of Engineering in Medicine, 09544119211026095. https://doi.org/10.1177/09544119211026095

28. Ali N, Zaman A, Sajid M, Bég O A, Shamshuddin M D, Kadir, A. (2018). Numerical simulation of time-dependent non-Newtonian nano-pharmacodynamic transport phenomena in a tapered overlapping stenosed artery. NanoSci Technol 2018: 9:2. https://doi.org/10.1615/NanoSciTechnolIntJ.2018027297
29. Haik Y, Pai V, Chen CJ. Apparent viscosity of human blood in a high static magnetic field. J Magn Magn Mater 2001;225:180-6. https://doi.org/10.1016/S0304-8853(00)01249-X
30. Yadav RP, Harminder S, Bhoopal S. Experimental studies on blood flow in stenosis arteries in presence of magnetic field. Ultra Sci. 2008;20:499-4.
31. Nadeem S, Ijaz S, Adil Sadiq M. Inspiration of induced magnetic field on a blood flow of Prandtl nanofluid model with stenosis. Curr Nanosci 2014;10:753-65. https://doi.org/10.2174/15734137106661406120103333
32. Ahmed A, Nadeem S. Effects of magnetohydrodynamics and hybrid nanoparticles on a micropolar fluid with 6-types of stenosis. Results Phys 2017;7:4130-9. https://doi.org/10.1016/j.rinp.2017.10.032
33. Zaman A, Sajid M, Kousar N. Biomedical study of effects nanoparticles on unsteady blood (non-Newtonian) flow through a catheterized stenotic vessel. Can J Phys 2019;97:487-97. https://doi.org/10.1139/cjp-2018-0376
34. Ismail Z, Abdullah I, Mustapha N, Amin N. A power-law model of blood flow through a tapered overlapping stenosed artery. Appl Math Comput 2008;195:669-80. https://doi.org/10.1016/j.amc.2007.05.014
35. Devi SA, Devi SS. Numerical investigation of hydromagnetic hybrid Cu–Al2O3/water nanofluid flow over a permeable stretching sheet with suction. Int J Nonlinear Sci Numer Simul 2016;17:249-57. https://doi.org/10.1515/ijnsns-2016-0037
36. Burton AC. Physiology and biophysics of the circulation: an introductory text. Year Book Medical Publishers; 1972.
37. Hoffman, K. A., Chiang, S. T. Computational Fluid Dynamics. Engineering Education System, 2000.
38. Zaman A, Ali N, Ali I. Effects of nanoparticles (Cu (Copper), Silver (Ag)) and slip on unsteady blood flow through a curved stenosed channel with aneurysm. Therm Sci Eng Prog 2018;5:482-91. https://doi.org/10.1016/j.tsep.2018.02.004
39. Zaman A, Ali N, Khan AA. Computational biomedical simulations of hybrid nanoparticles on unsteady blood hemodynamics in a stenotic artery. Math Comput Simul 2020;169:117-32. https://doi.org/10.1016/j.matcom.2019.09.010
40. Bég OA, Ali N, Zaman A, Bég ET, Sohail A. Computational modeling of heat transfer in an annular porous medium solar energy absorber with the P1-radiative differential approximation. J Taiwan Inst Chem Eng 2016;66:258-68. https://doi.org/10.1016/j.jtice.2016.06.034
41. Bég OA, Zaman A, Ali N, Gaffar SA, Bég ET. Numerical computation of nonlinear oscillatory two-immiscible magnetohydrodynamic flow in dual porous media system: FTCS and FEM study. Heat Tran Asian Res 2019;48:1245-63. https://doi.org/10.1002/htj.21429
42. Zaman A, Ali N, Bég OA. Numerical study of unsteady blood flow through a vessel using Sisko model. Int J Eng Sci Technol 2016;19:538-47. https://doi.org/10.1016/j.jestch.2015.09.013
43. Ali N, Javid K, Sajid M, Anwar Bég O. Numerical simulation of peristaltic flow of a biorheological fluid with shear-dependent viscosity in a curved channel. Comput Methods Biomech Biomed Eng. 2016;19:614-27. https://doi.org/10.1080/10255842.2015.1055257
44. Zaman A, Ali N, Bég OA, Sajid M. Heat and mass transfer to blood flowing through a tapered overlapping stenosed artery. Int J Heat Mass Transfer. 2016;95:1084-95. https://doi.org/10.1016/j.ijheatmasstransfer.2015.12.073
45. Ali N, Javed MA, Bég OA, Hayat T. Mathematical model for isothermal wire-coating from a bath of Giesekus viscoelastic fluid. Chem Eng Commun 2016; 203: 1336-48. https://doi.org/10.1080/00986445.2016.1194272
46. Ijaz S, Nadeem S. Examination of nanoparticles as a drug carrier on blood flow through catheterized composite stenosed artery with permeable walls. Comput Methods Programs Biomed 2016;133:83-94. https://doi.org/10.1016/j.cmpb.2016.05.004

47. Tripathi D, Sharma A, Anwar Bég O, Tiwari A. Electrothermal transport in biological systems: an analytical approach for electrokinetically modulated peristaltic flow. J Therm Sci Eng Appl 2017;9:041010. https://doi.org/10.1115/1.4036803

48. Roy AK, Bég OA. Mathematical modelling of unsteady solute dispersion in two-fluid (micropolar-Newtonian) blood flow with bulk reaction. Int Commun Heat Mass Transf 2021;122:105169. https://doi.org/10.1016/j.icheatmasstransfer.2021.105169

49. Zaman, A., Ali, N., & Bég, O. A. (2016). Unsteady magnetohydrodynamic blood flow in a porous-saturated overlapping stenotic artery—numerical modeling. Journal of Mechanics in Medicine and Biology, 16(04), 1650049. https://doi.org/10.1142/S0219519416500494

50. Akbar, N. S., & Butt, A. W. (2015). Magnetic field effects for copper suspended nanofluid venture through a composite stenosed arteries with permeable wall. Journal of Magnetism and magnetic materials, 381, 285-291. https://doi.org/10.1016/j.jmmm.2014.12.084

51. Lekshmi, K. M., Che, H. L., Cho, C. S., & Park, I. K. (2017). Drug-and gene-eluting stents for preventing coronary restenosis. Chonnam medical journal, 53(1), 14-27. https://doi.org/10.4068/cmj.2017.53.1.14

Figures and Tables

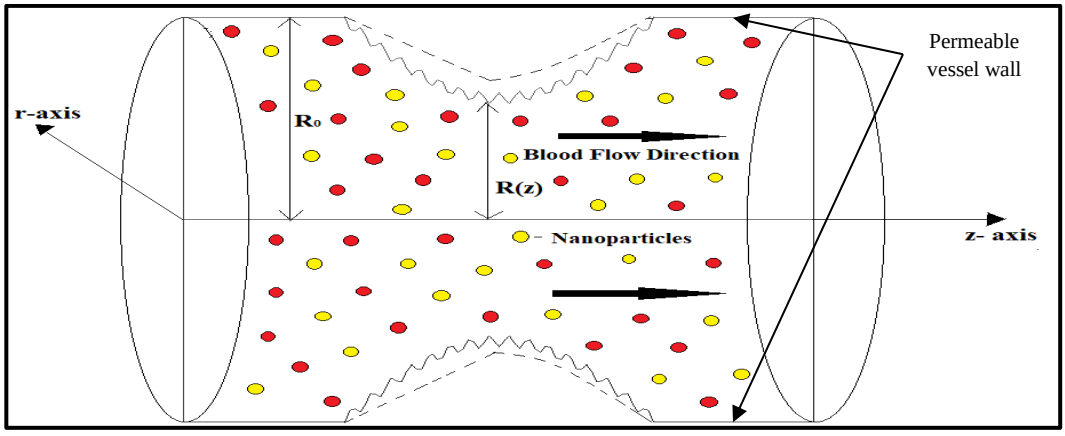

Figure 1 (a): Geometry of the artery with two differently shaped stenosis

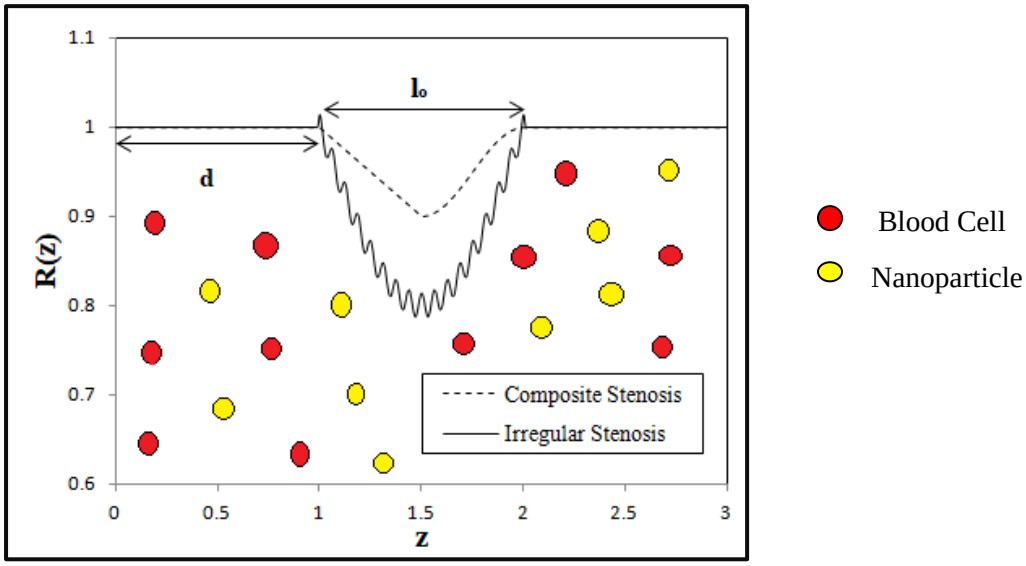

Figure 1(b): Geometry of the stenotic arterial segment where d is distance from origin and l_0 is total stenotic length

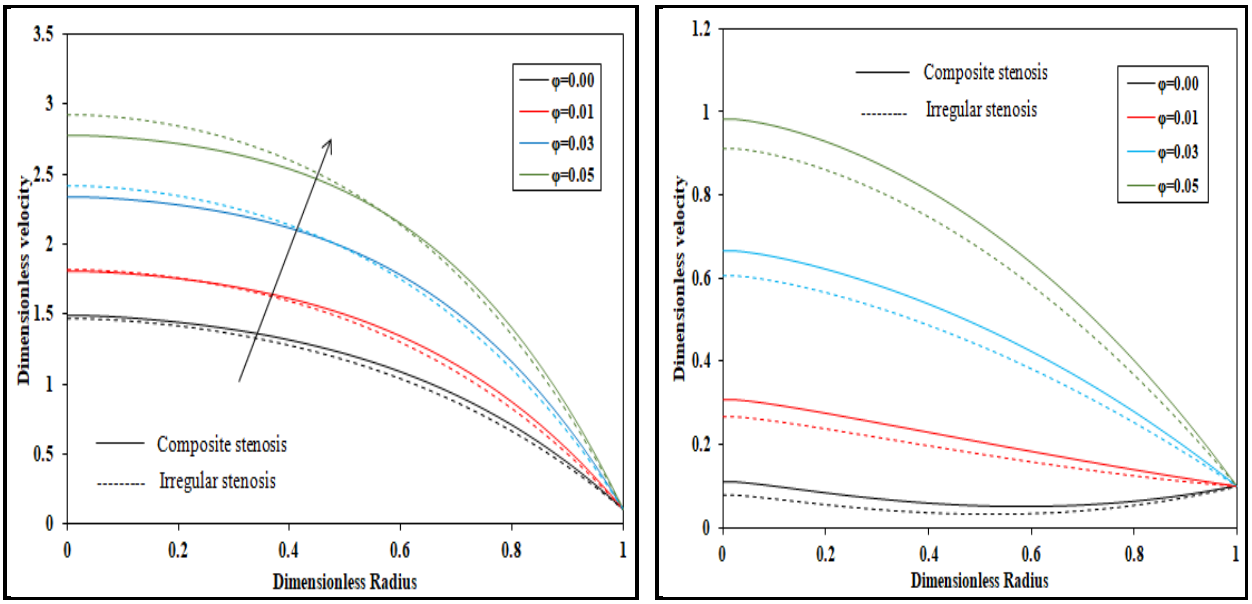

Figure 2: Effect of nanoparticle concentration on axial velocity for (a) n=1.5 (b) n=0.5 through two different stenosis at $B_1 = 1.41, \delta = 0.1, z = 1.5, t = 1.2$

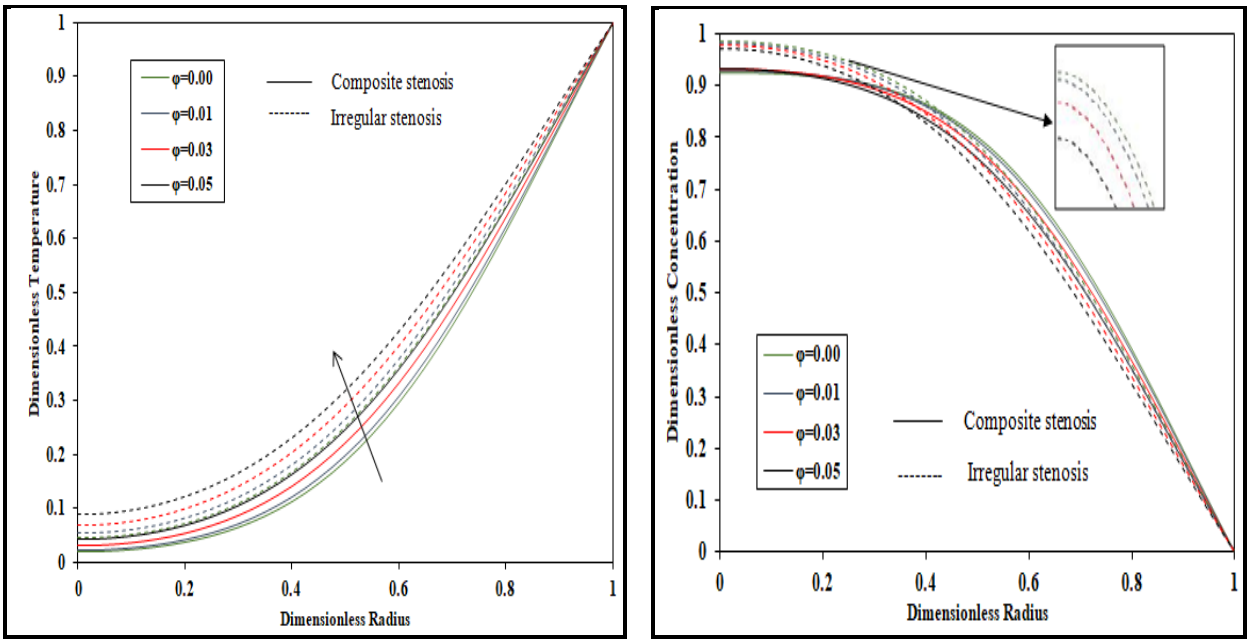

Figure 3: Effect of nanoparticle volume fraction on (a) temperature and (b) concentration profiles through two different stenosis at $B_1 = 1.41, \delta = 0.1, z = 1.5, t = 1.2$

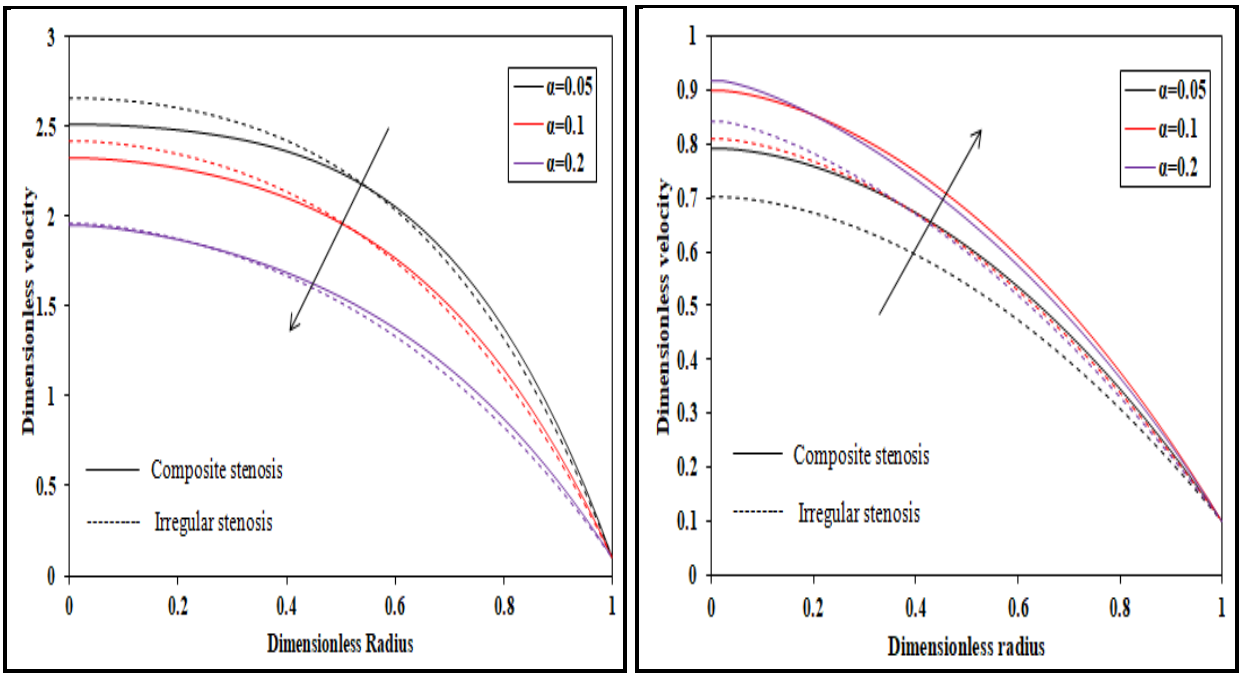

Figure 4: Effect of various α on velocity profile for (a) n=1.5 and (b) n=0.5 through two different stenosis at $B_1 = 1.41, \delta = 0.1, z = 1.5, t = 1.2$

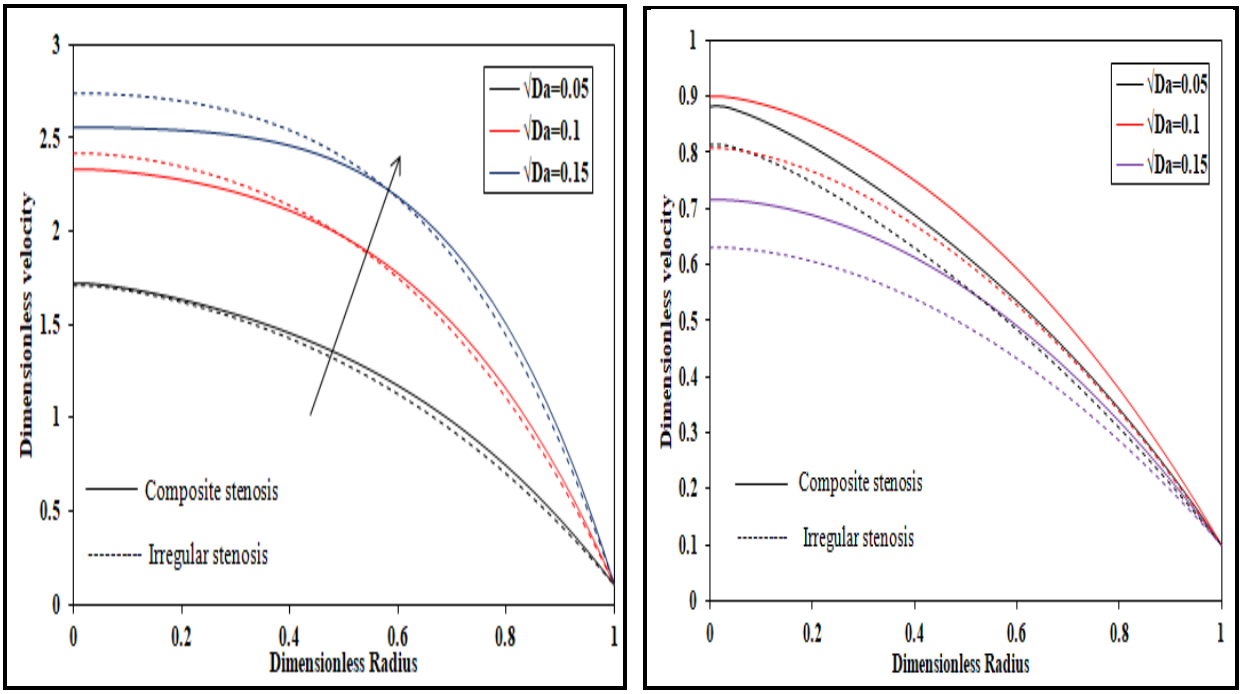

Figure 5: Effect of various √Da values on velocity profiles for (a) *n*=1.5 and (b) *n*=0.5 through two different stenosis at $B_1 = 1.41, \delta = 0.1, z = 1.5, t = 1.2$

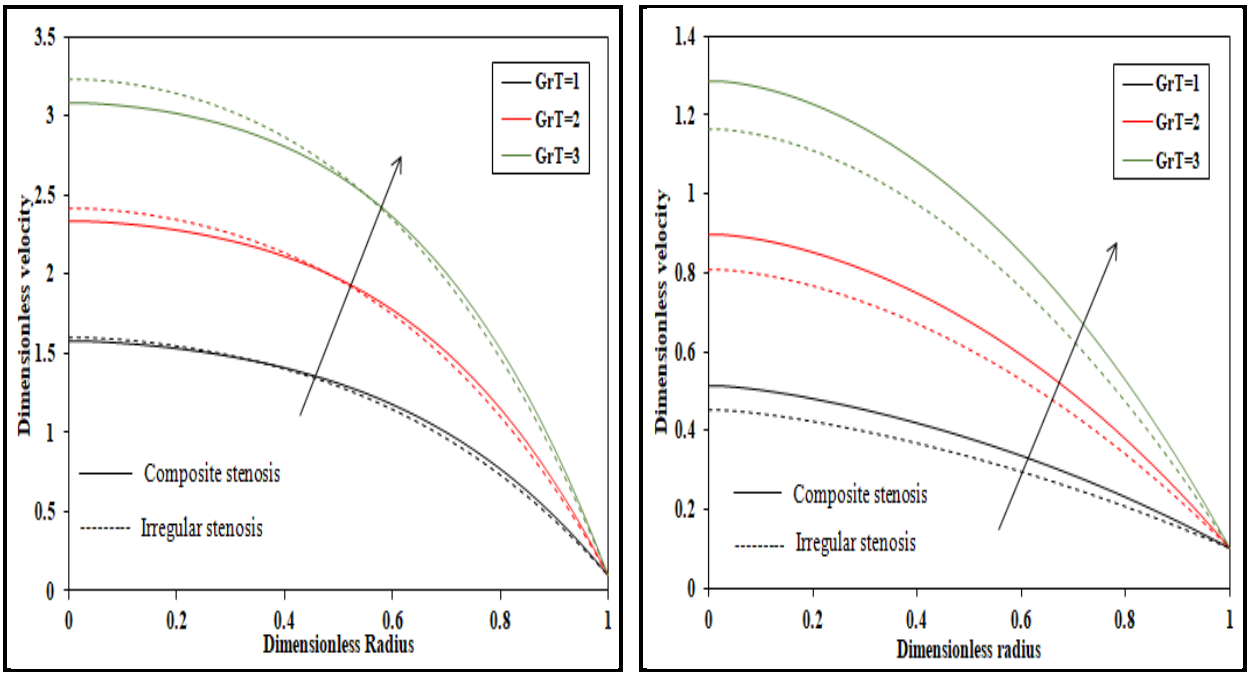

Figure 6: Effect of various Gr_T values (thermal Grashof number) on velocity profile for (a) n=1.5 and (b) n=0.5 and through two different stenosis at $B_1 = 1.41, \delta = 0.1, z = 1.5, t = 1.2$

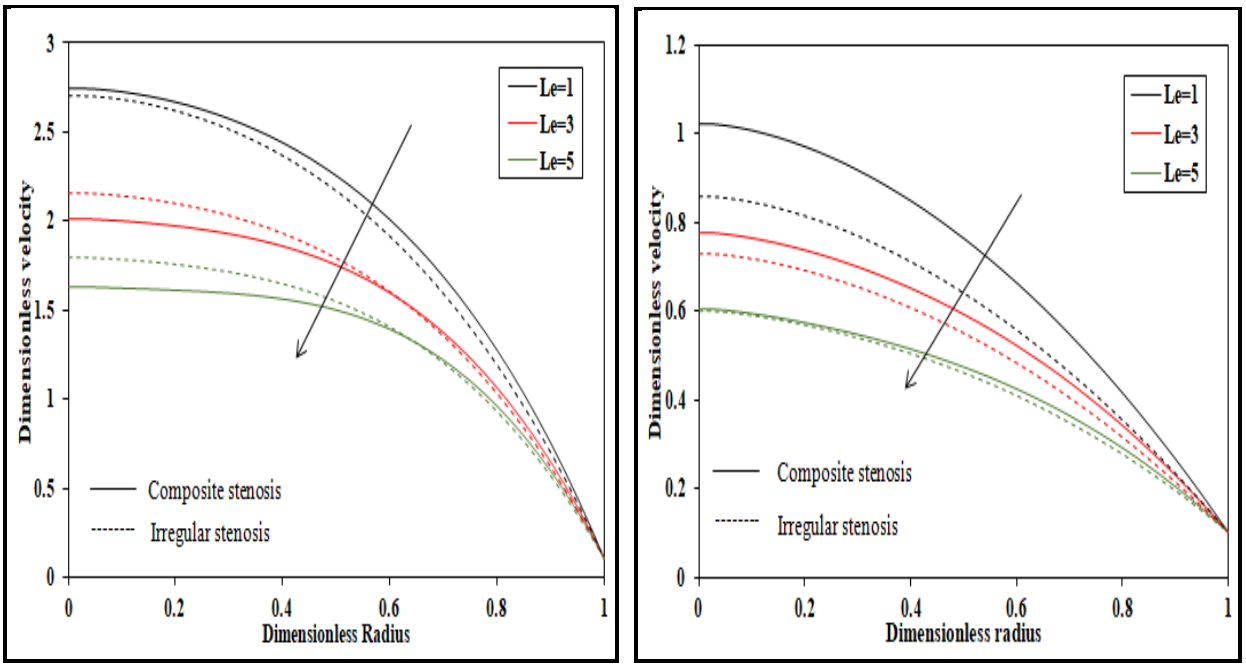

Figure 7: Effect of various Le values on velocity profiles for (a) n=1.5 and (b) n=0.5 and through two different stenosis at $B_1 = 1.41, \delta = 0.1, z = 1.5, t = 1.2$

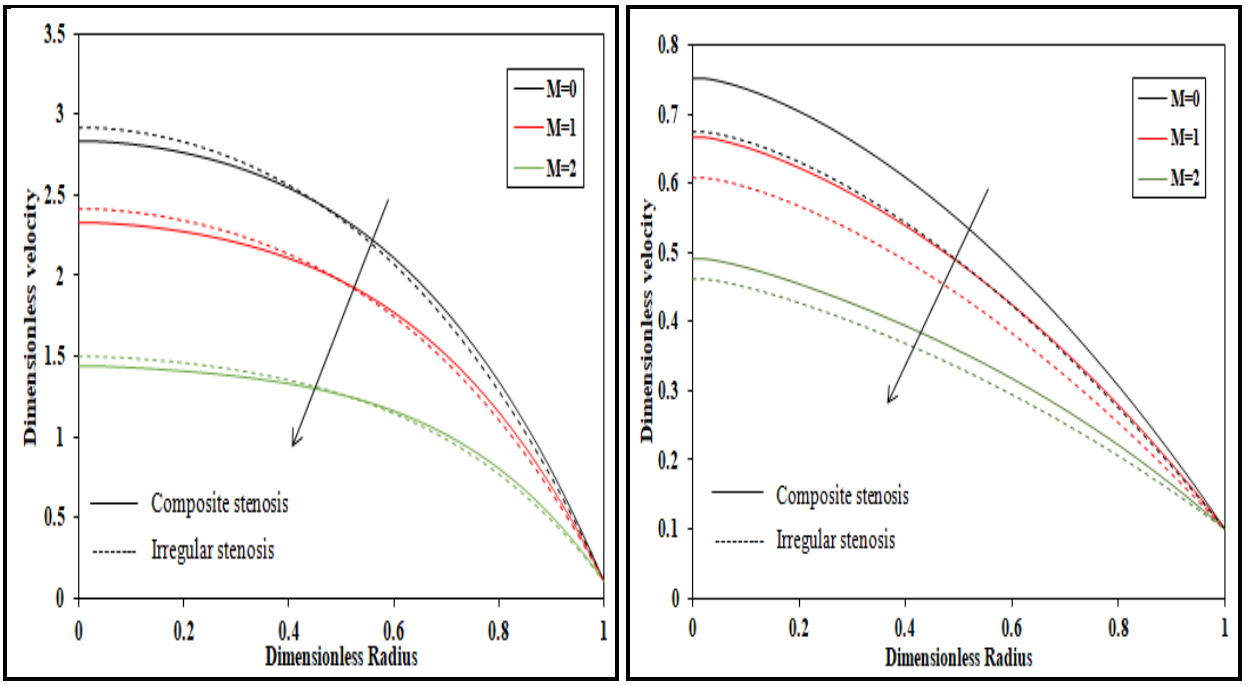

Figure 8: Effect of various *M* values on velocity profiles for (a) *n*=1.5 and (b) *n*=0.5 through two different stenosis at $B_1 = 1.41, \delta = 0.1, z = 1.5, t = 1.2$

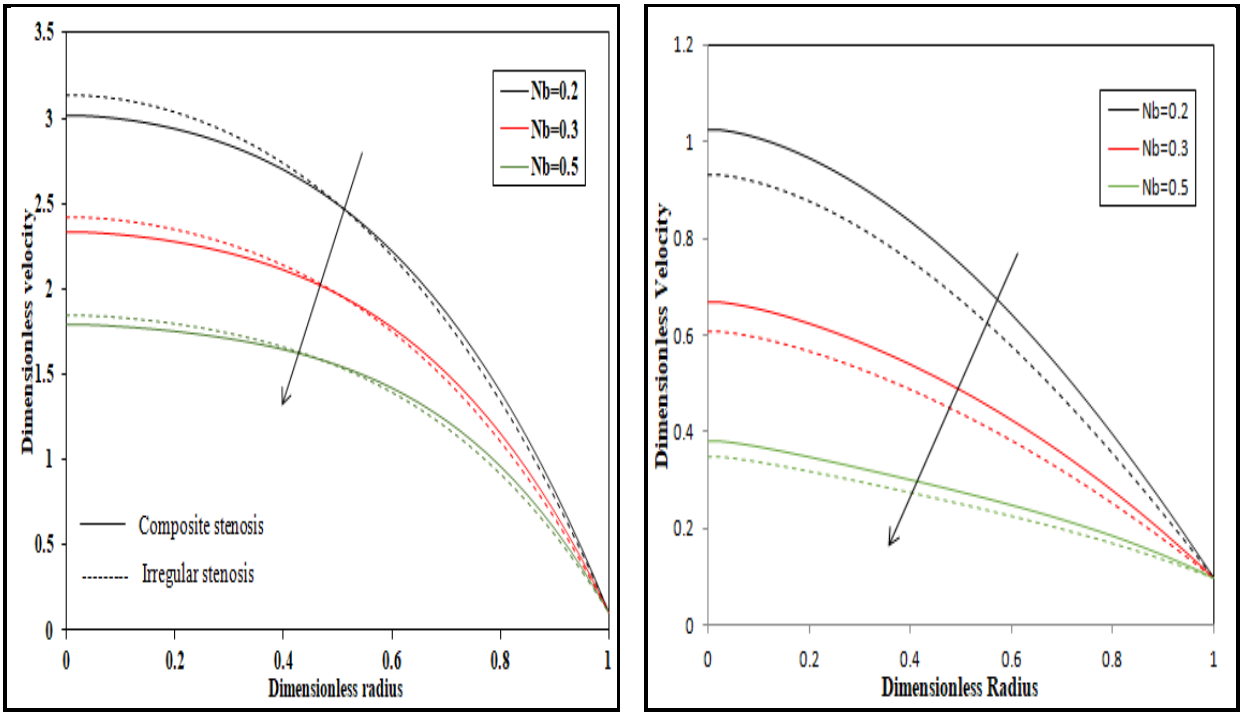

Figure 9: Effect of various *Nb* values on velocity profile for (a) *n*=1.5 and (b) *n*=0.5 through two different stenosis at $B_1 = 1.41, \delta = 0.1, z = 1.5, t = 1.2$

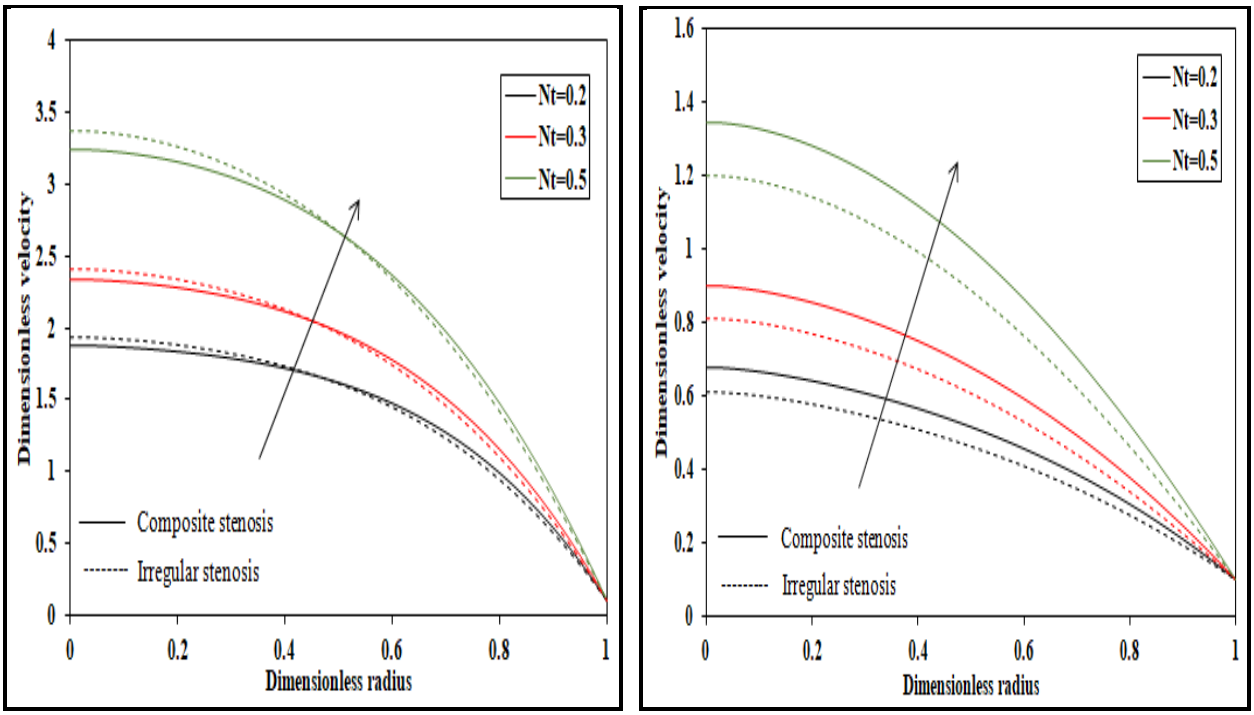

Figure 10: Effect of various Nt on velocity profile for (a) n=1.5 and (b) n=0.5 through two different stenosis at $B_1 = 1.41, \delta = 0.1, z = 1.5, t = 1.2$

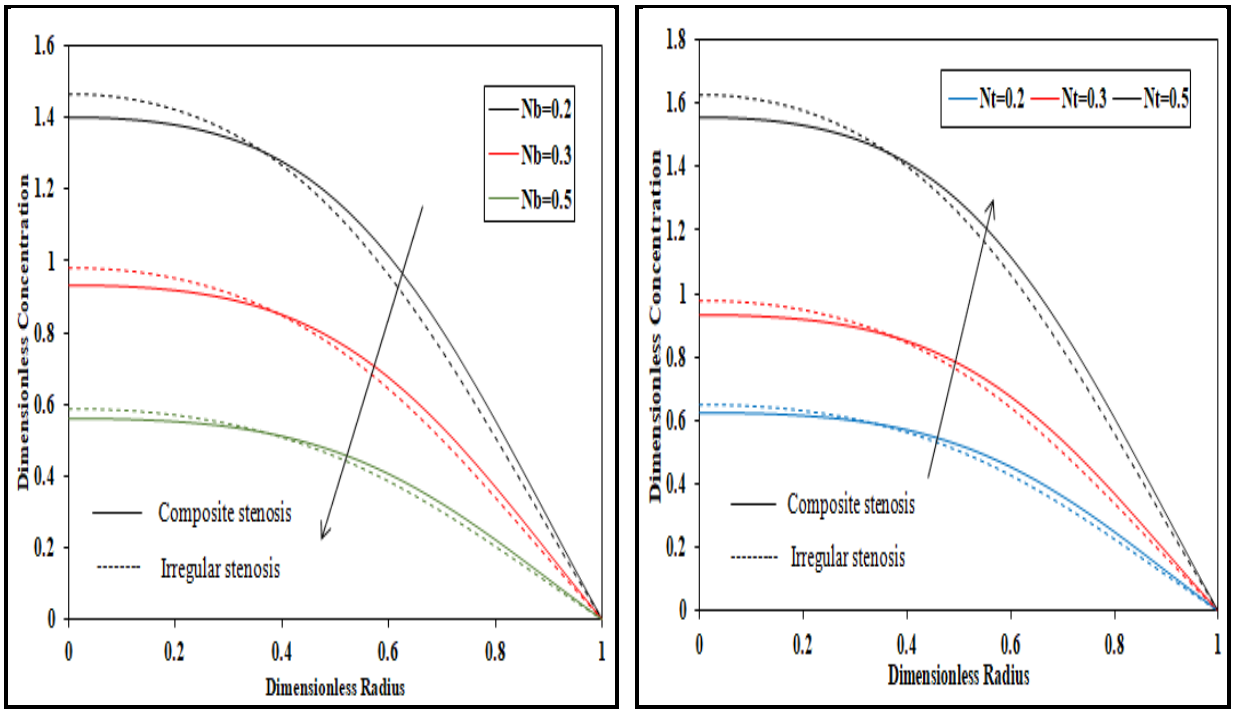

Figure 11: Effect on nano-particle concentration profiles for (a) various *Nb* values and (b) various *Nt* values for two different stenosis at $B_1 = 1.41, \delta = 0.1, z = 1.5, t = 1.2$

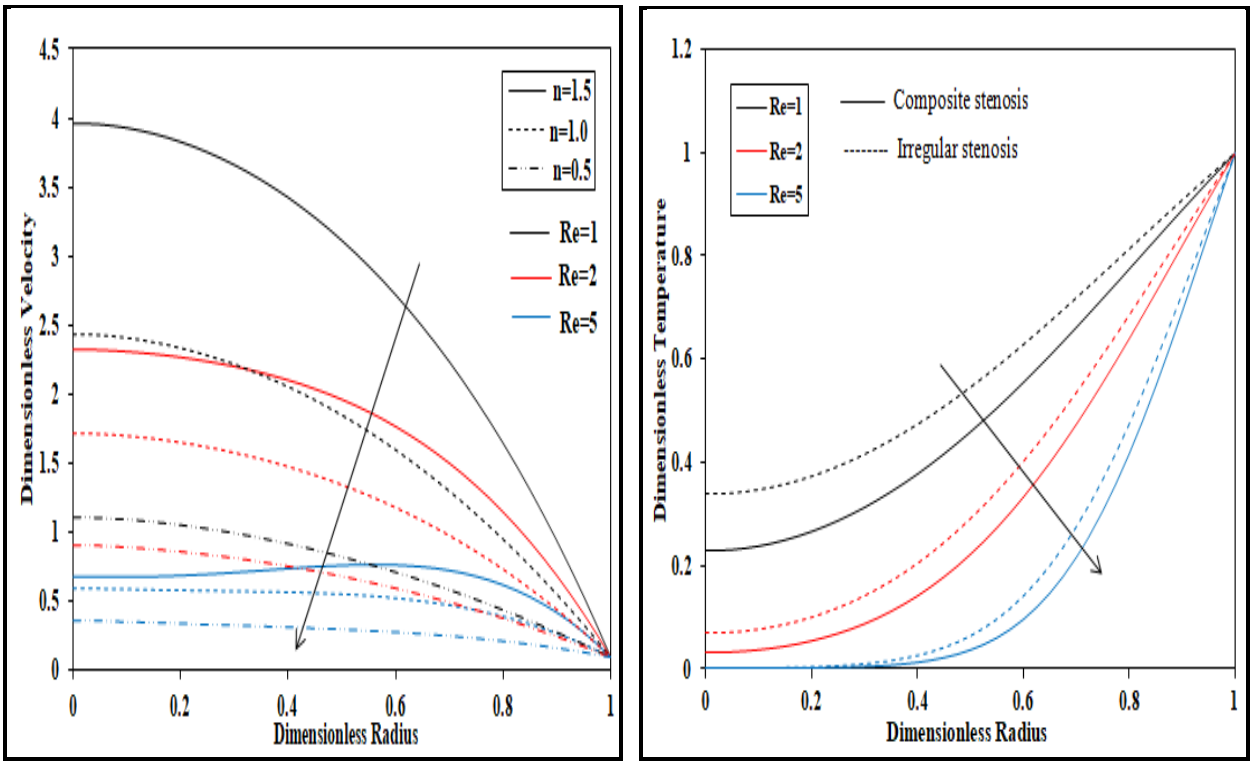

Figure 12: Effect of various *Re* values on (a) velocity and (b) temperature profiles in two different stenosis at $B_1 = 1.41, \delta = 0.1, z = 1.5, t = 1.2$

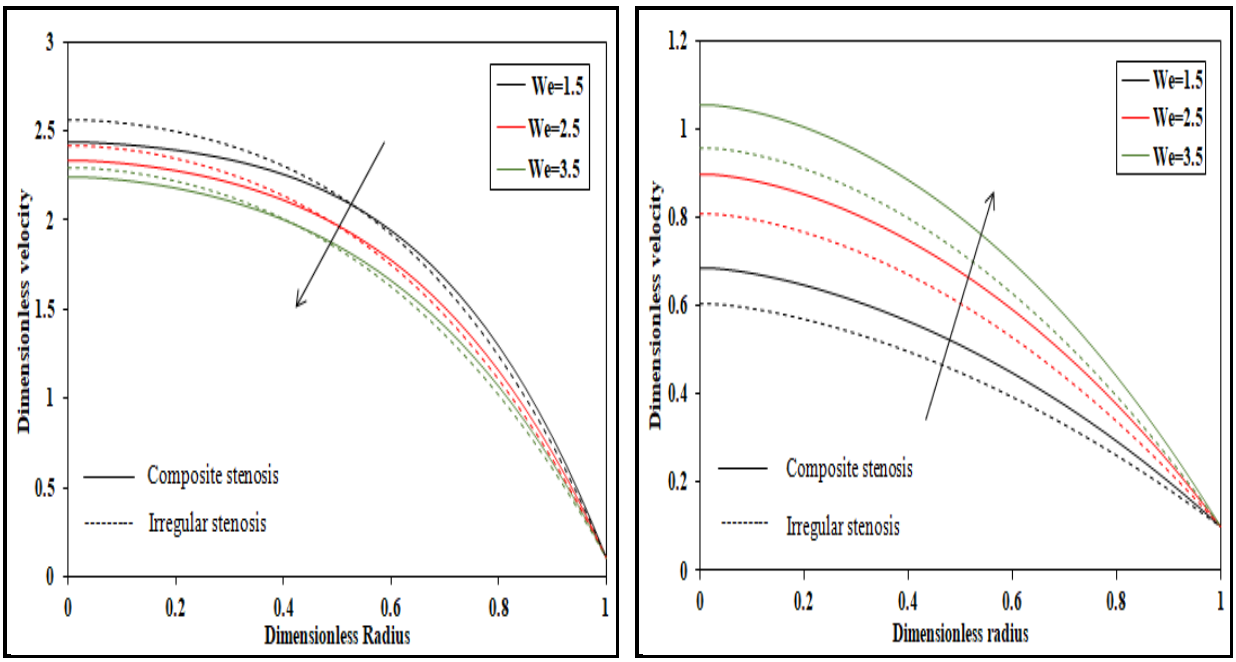

Figure 13: Effect of various *We* values on velocity profile for (a) *n*=1.5 and (b) *n*=0.5 through two different stenosis at $B_1 = 1.41, \delta = 0.1, z = 1.5, t = 1.2$

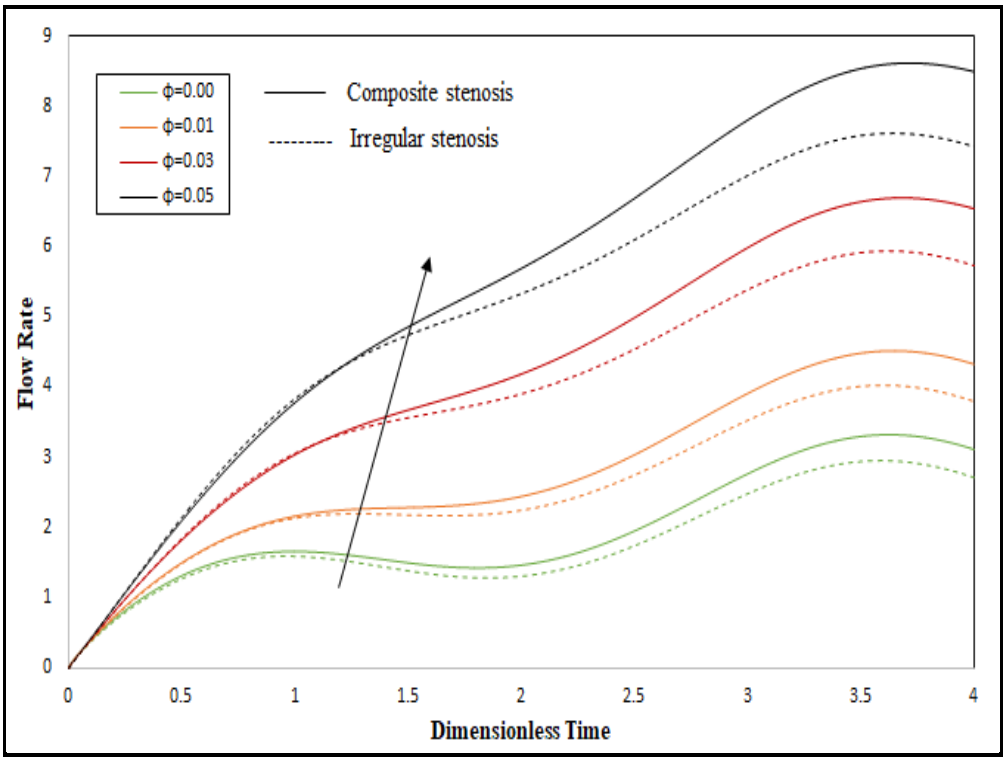

Figure 14: Effect of nanoparticle concentration on flow rate for n=1.5 through two different stenosis at $B_1 = 1.41, \delta = 0.1, z = 1.5$

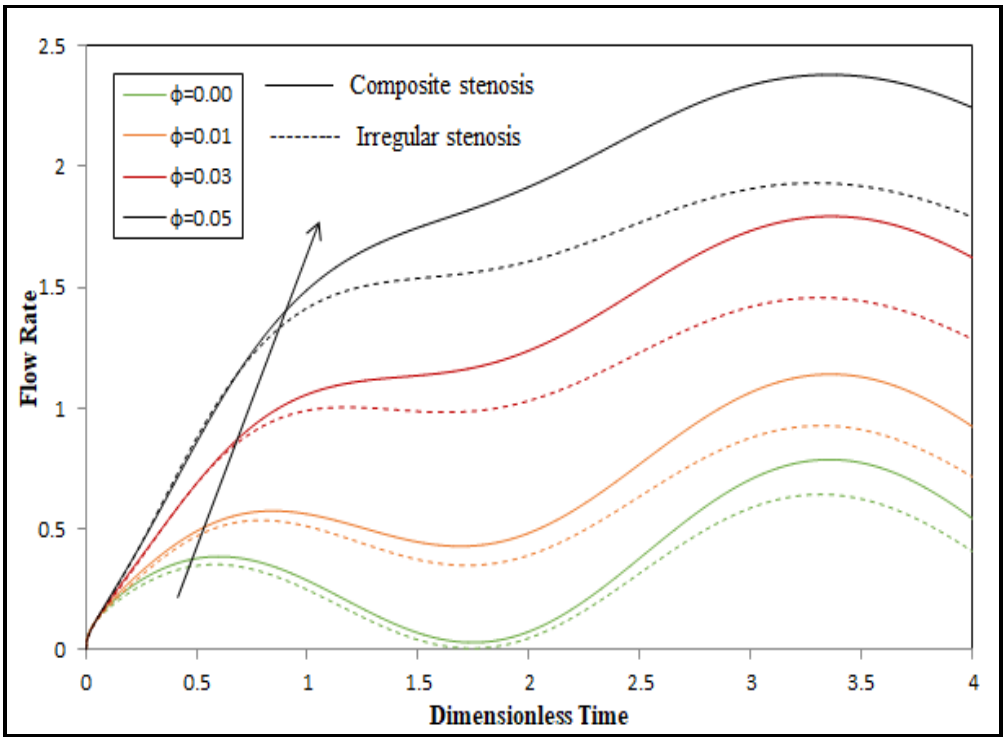

Figure 15: Effect of nanoparticle volume fraction on volumetric flow rate for n = 0.5 through two different stenosis at $B_1 = 1.41, \delta = 0.1, z = 1.5$

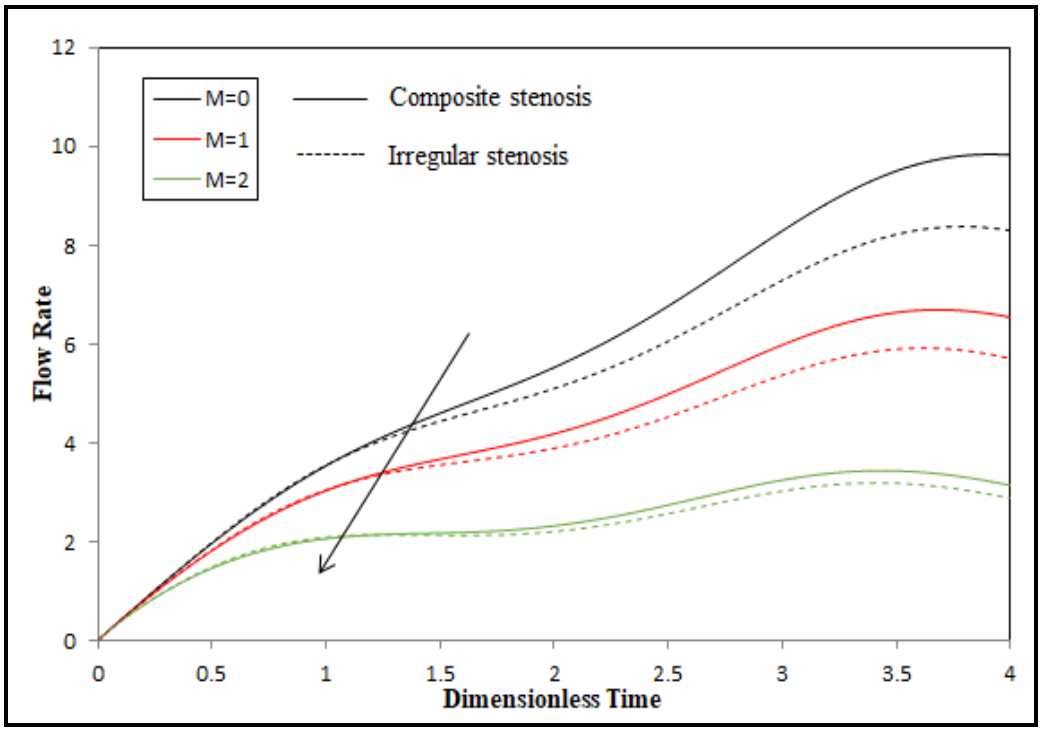

Figure 16: Effect of magnetic Hartmann number on volumetric flow rate for n = 1.5 through two different stenosis at $B_1 = 1.41, \delta = 0.1, z = 1.5$

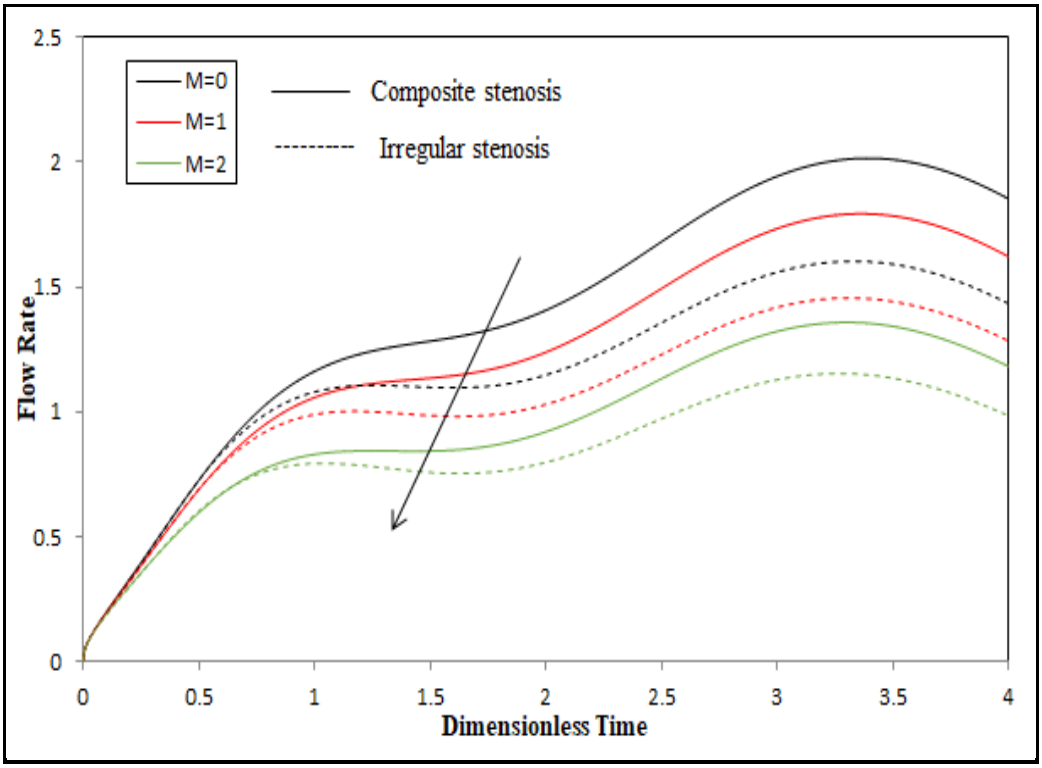

Figure 17: Effect of magnetic Hartmann number on volumetric flow rate for n = 0.5 through two different stenosis at $B_1 = 1.41, \delta = 0.1, z = 1.5$

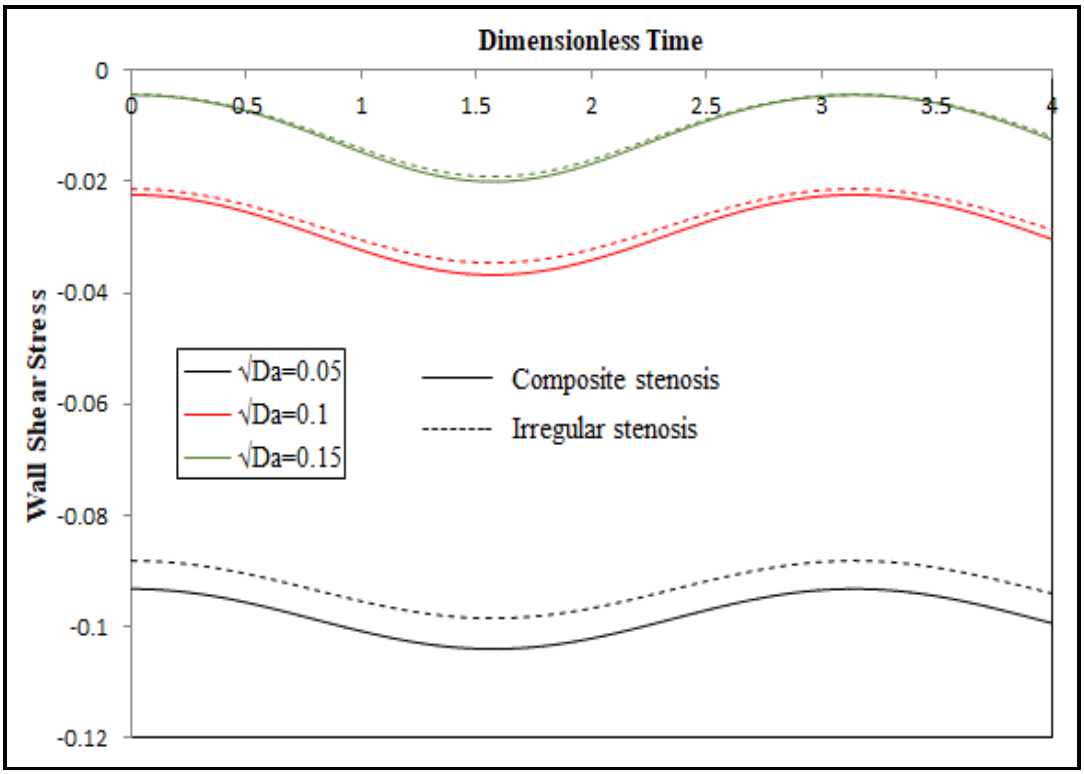

Figure 18: Effect of *Da* values on wall shear stress for *n*=1.5 through two different stenosis at $B_1 = 1.41, \delta = 0.1, z = 1.5$

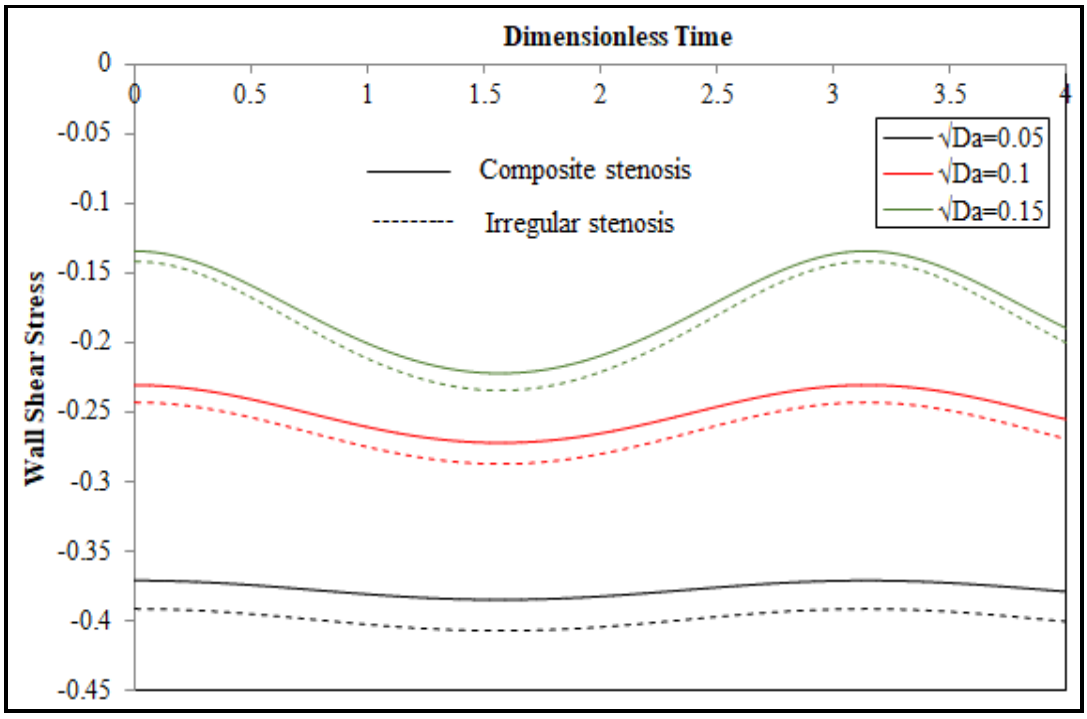

Figure 19: Effect of *Da* values on wall shear stress for *n* = 0.5 through two different stenosis at $B_1 = 1.41, \delta = 0.1, z = 1.5$

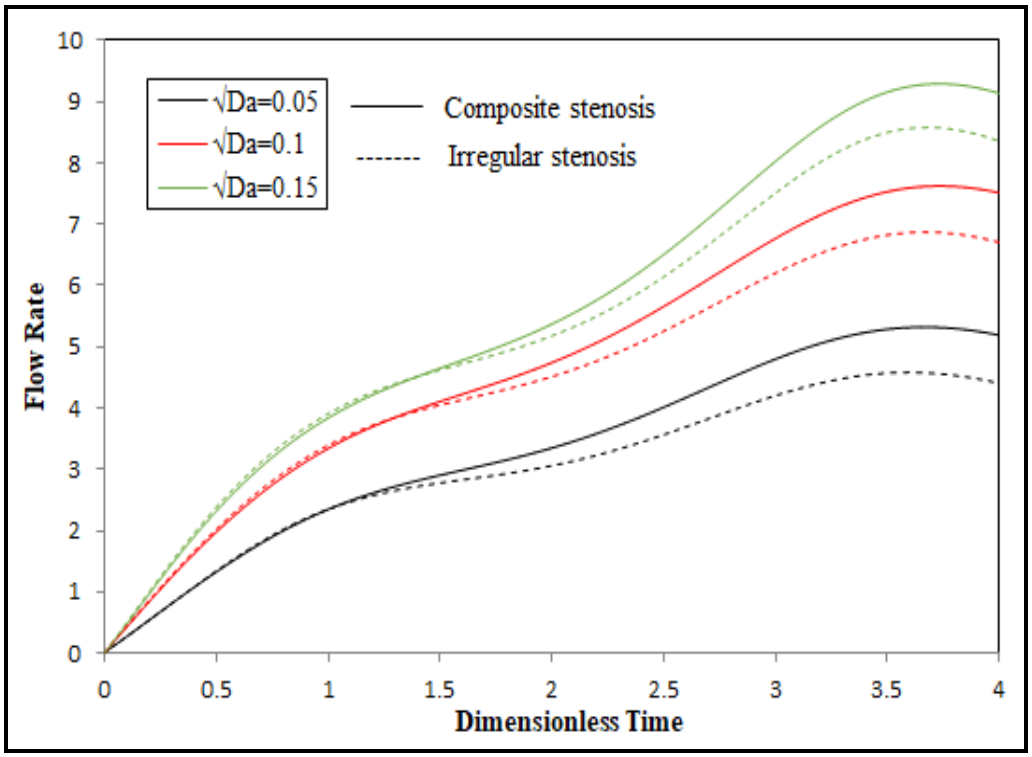

Figure 20: Effect of *Da* values on volumetric flow rate for n = 1.5 through two different stenosis at $B_1 = 1.41, \delta = 0.1, z = 1.5$

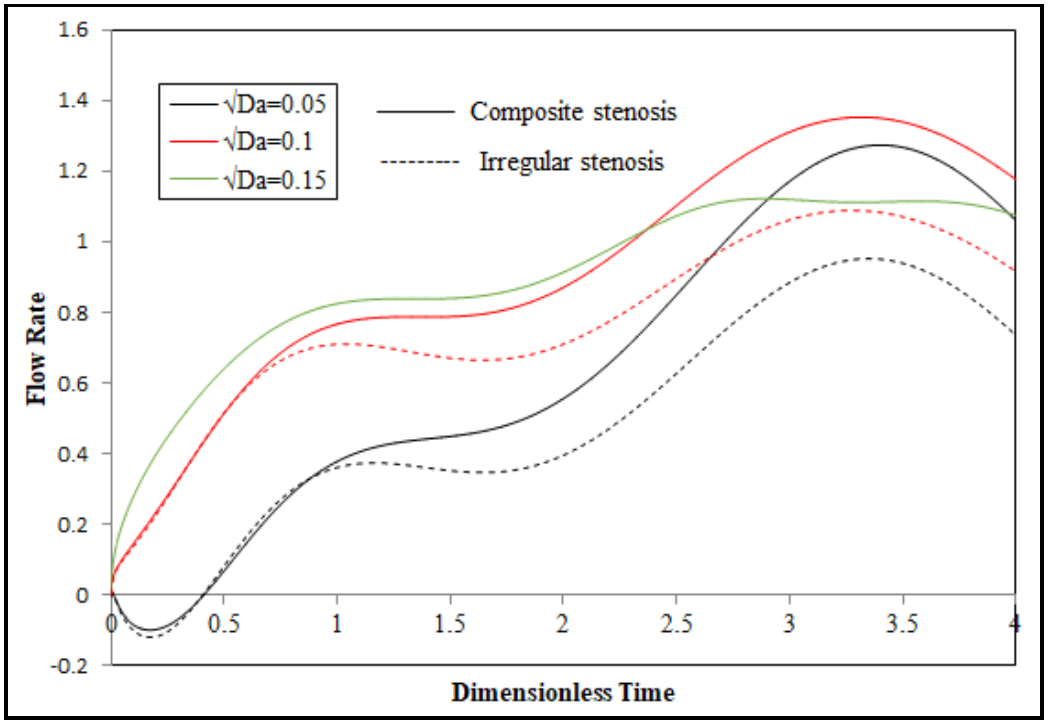

Figure 21: Effect of *Da* values on volumetric flow rate for n = 0.5 through two different stenosis at $B_1 = 1.41, \delta = 0.1, z = 1.5$

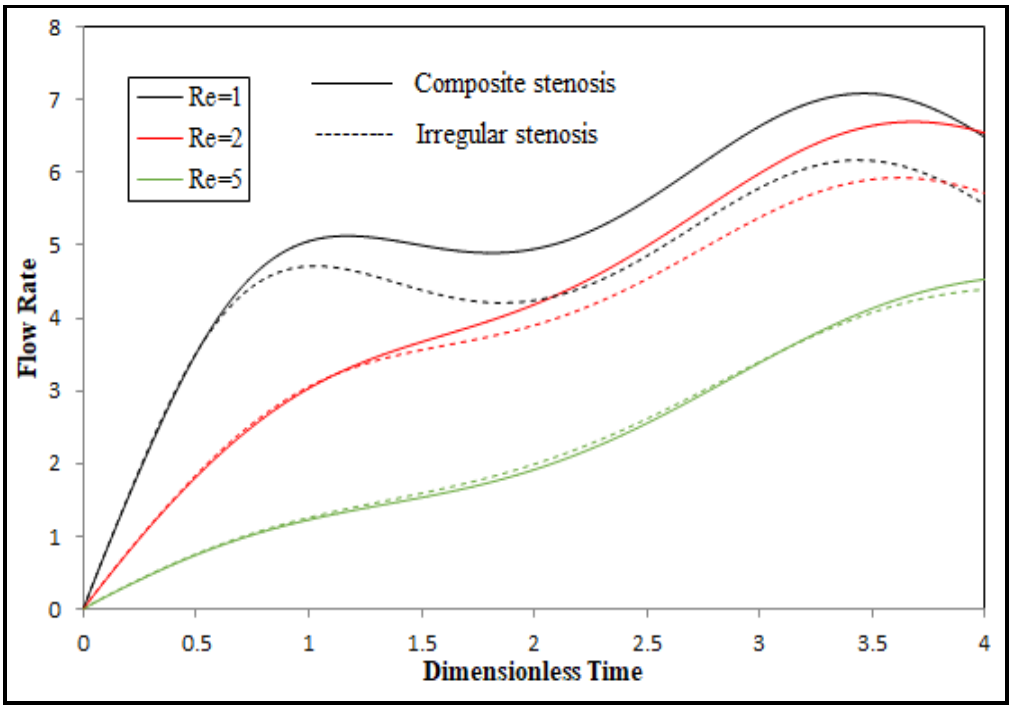

Figure 22: Effect of *Re* values on volumetric flow rate for n = 1.5 through two different stenosis at $B_1 = 1.41, \delta = 0.1, z = 1.5$

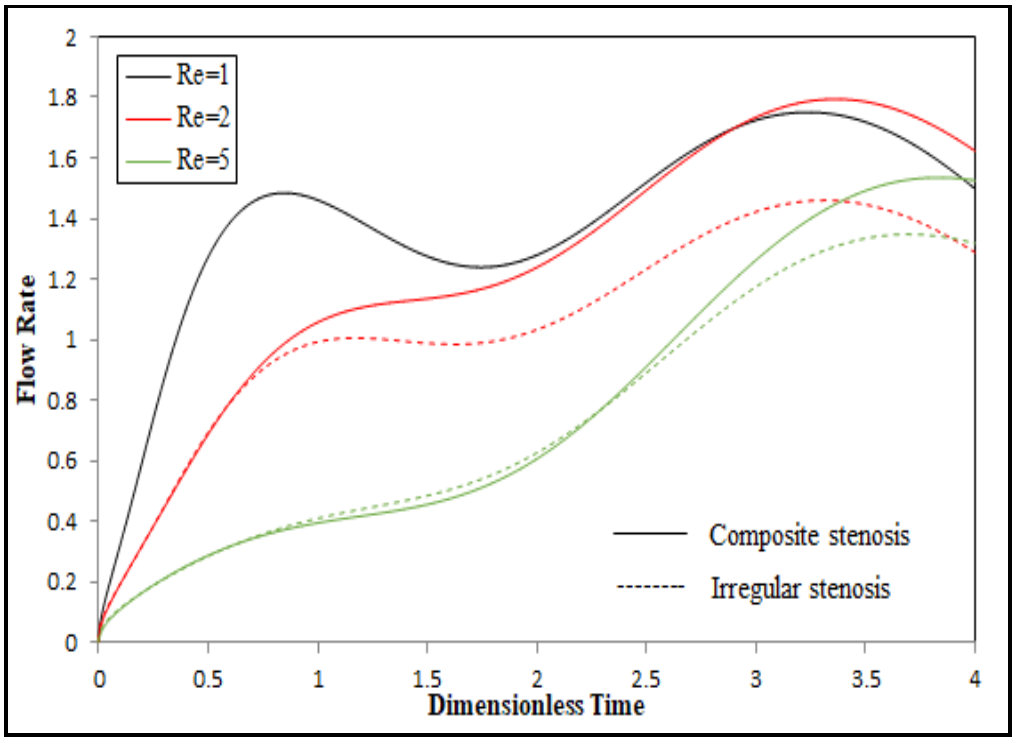

Figure 23: Effect of *Re* values on flow rate for n = 0.5 through two different stenosis at $B_1 = 1.41, \delta = 0.1, z = 1.5$

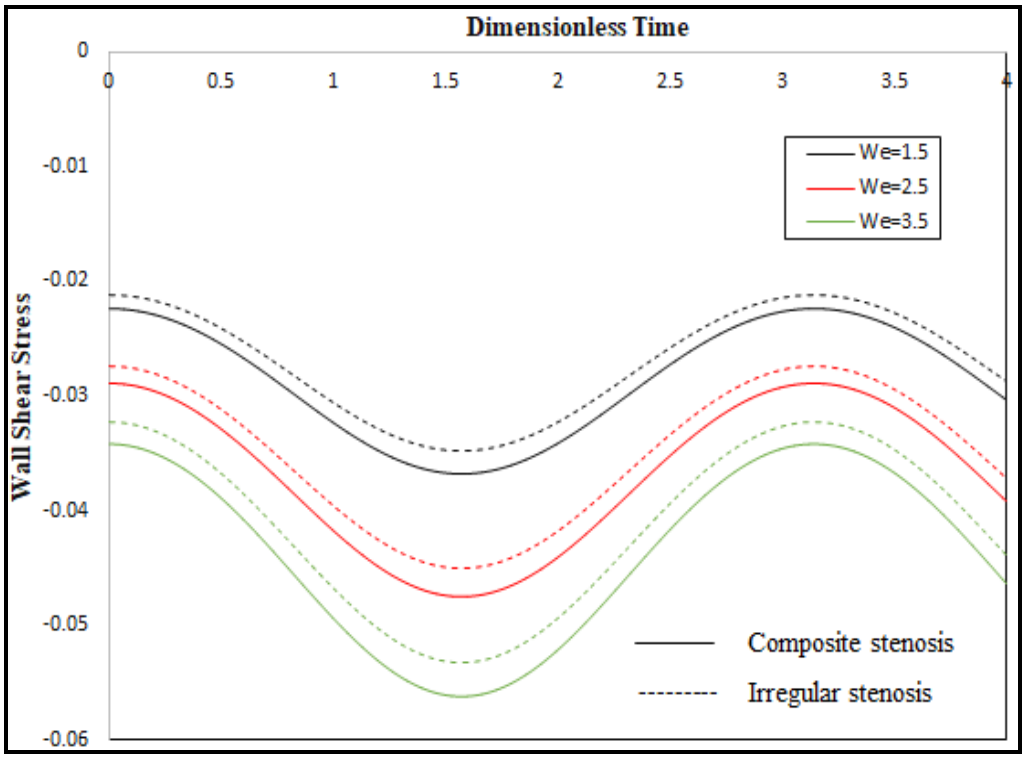

Figure 24: Effect of *We* values on wall shear stress for n = 1.5 through two different stenosis at $B_1 = 1.41, \delta = 0.1, z = 1.5$

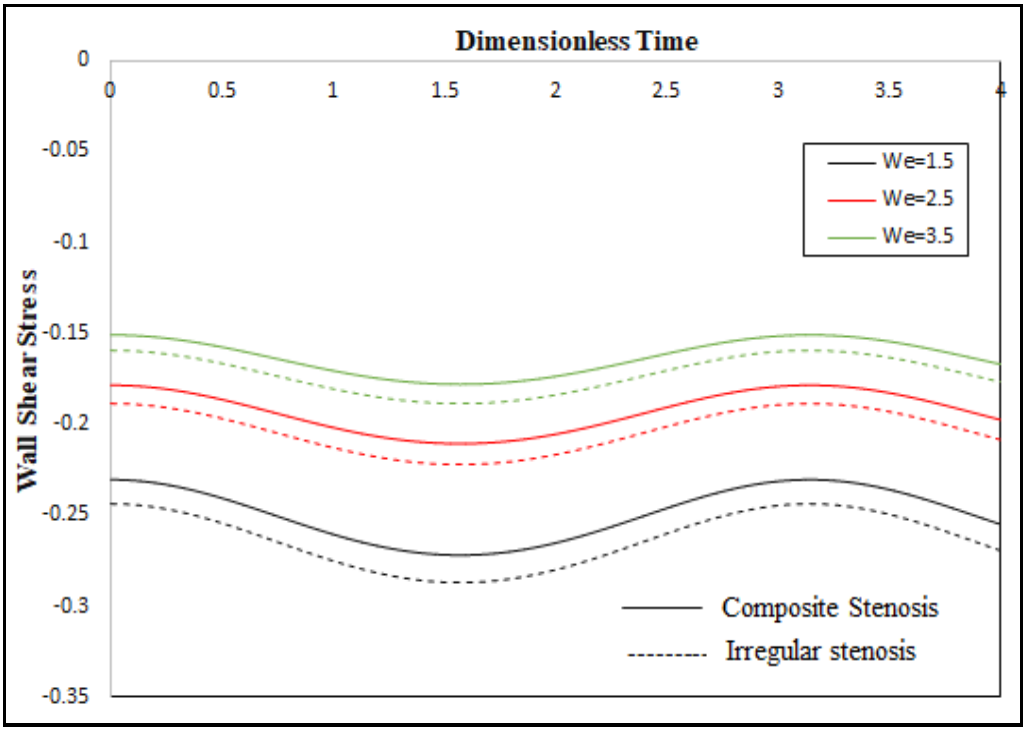

Figure 25: Effect of *We* values on wall shear stress for n = 0.5 through two different stenosis at $B_1 = 1.41, \delta = 0.1, z = 1.5$

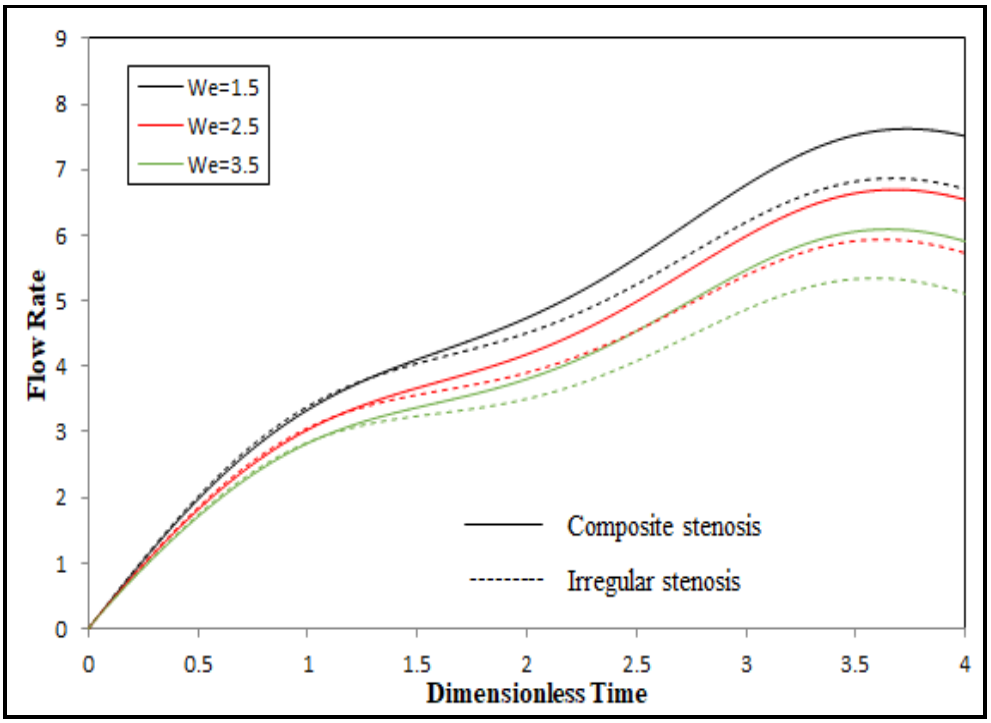

Figure 26: Effect of *We* values on volumetric flow rate for n = 1.5 through two different stenosis at $B_1 = 1.41, \delta = 0.1, z = 1.5$

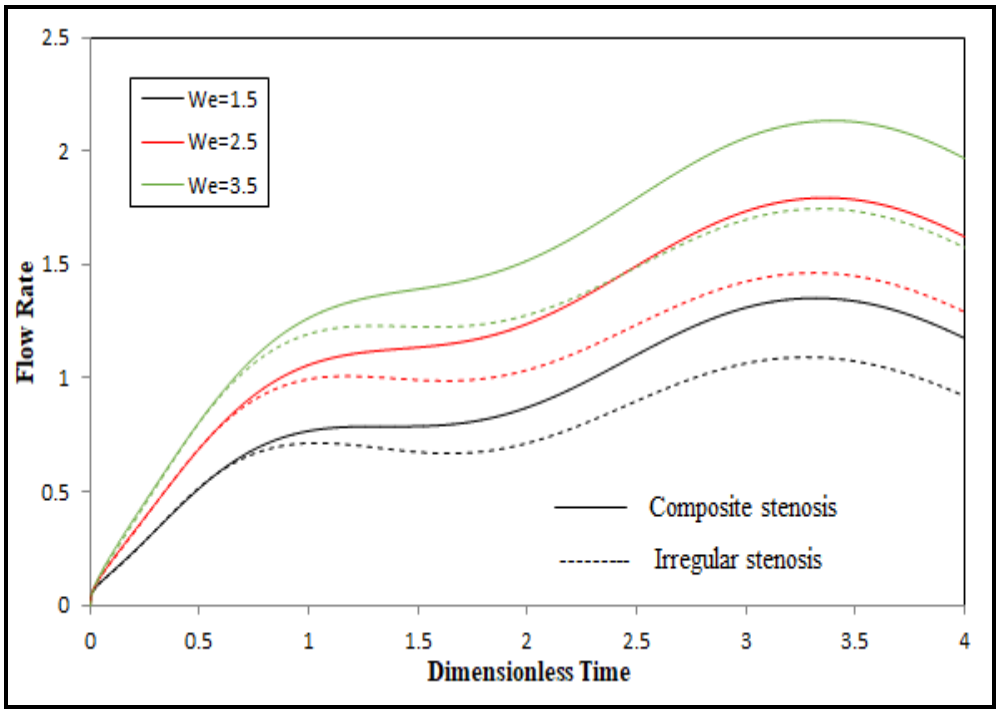

Figure 27: Effect of *We* values on volumetric flow rate for n = 0.5 through two different stenosis at $B_1 = 1.41, \delta = 0.1, z = 1.5$

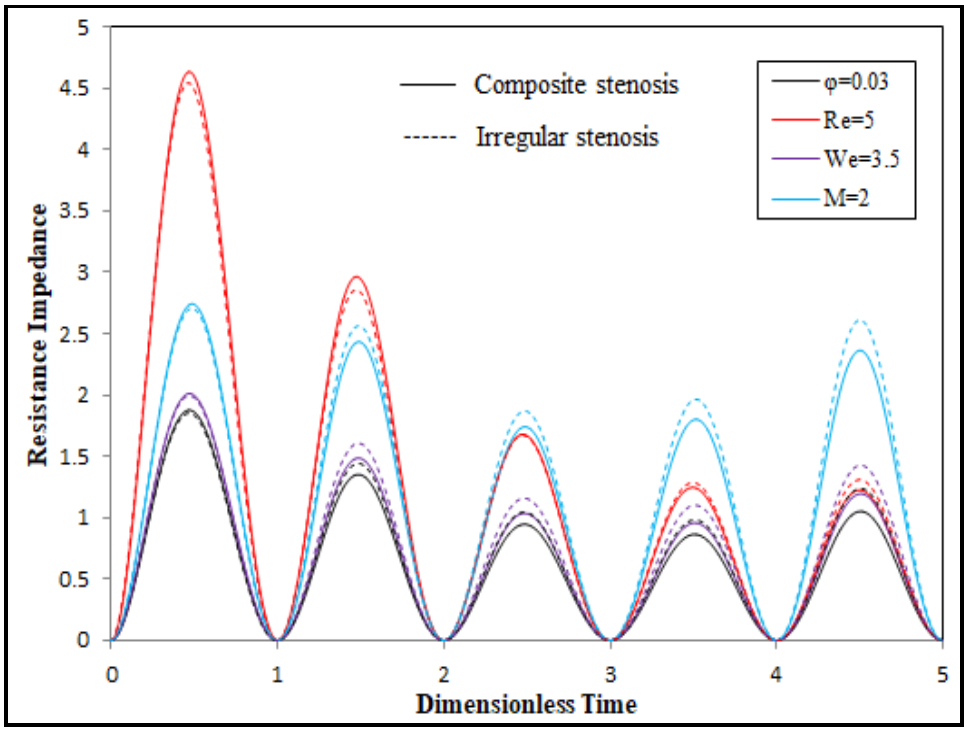

Figure 28: Time variation of resistance impedance for n = 1.5 through two different stenosis with other default parameter values

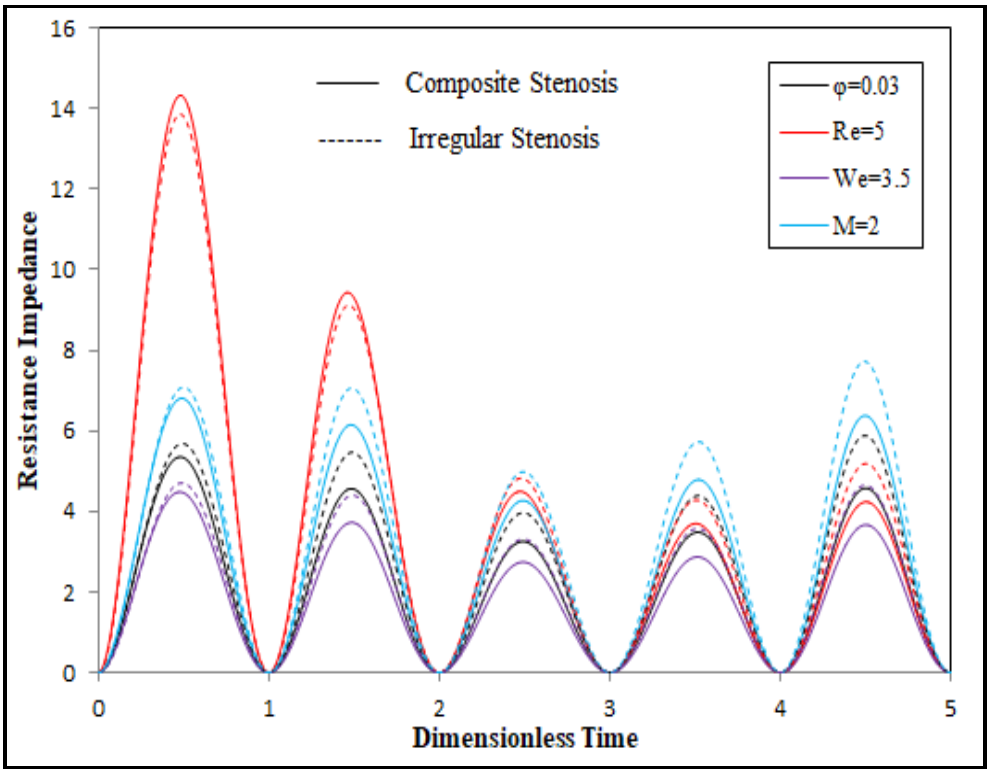

Figure 29: Time variation of resistance impedance for n = 0.5 through two different stenosis with other default parameter values

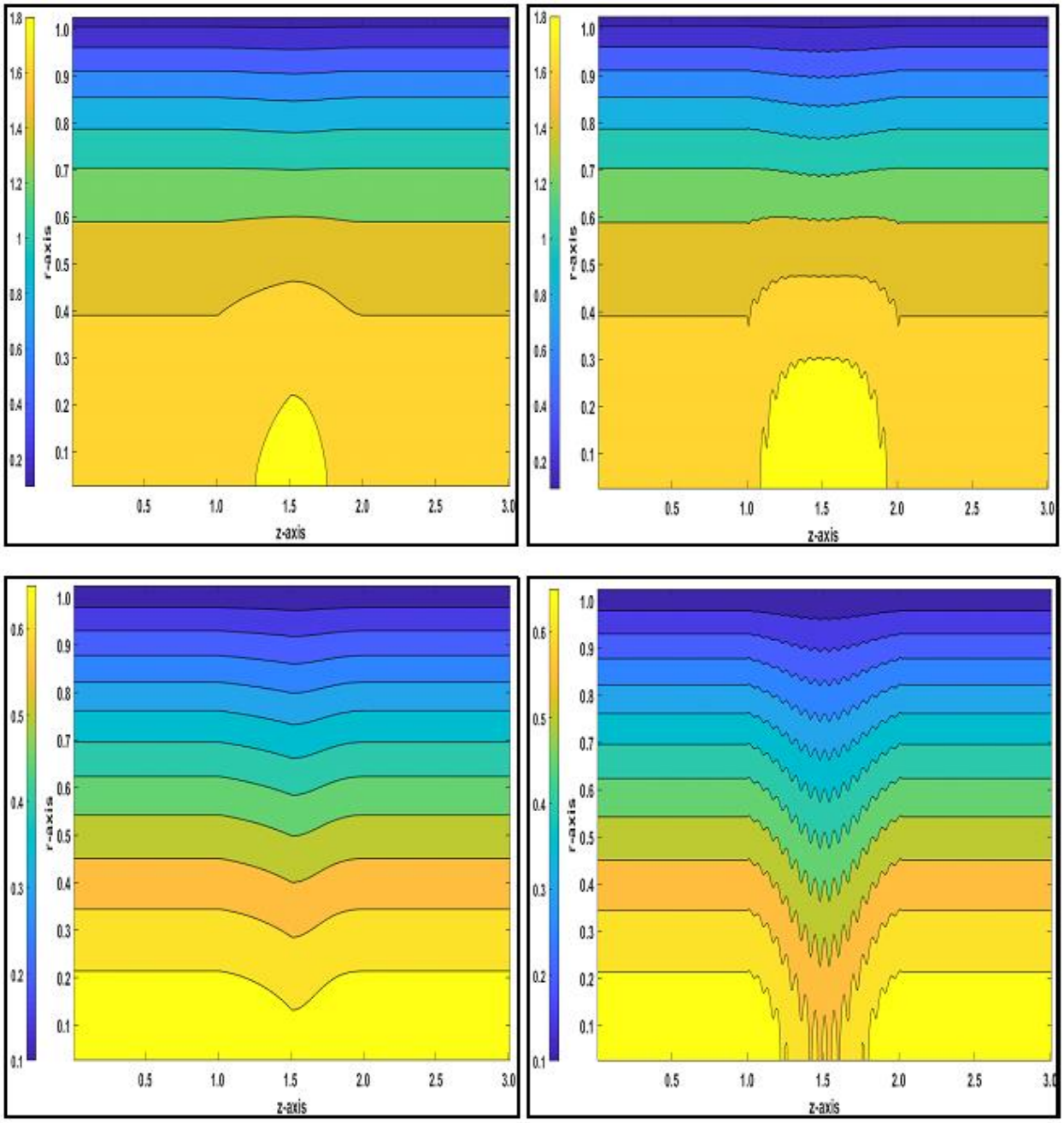

Figure 30: Blood Flow pattern along the axial direction with the following data

(a) For default parameter values through composite and irregular stenoses and for *n=1.5, n=0.5* respectively

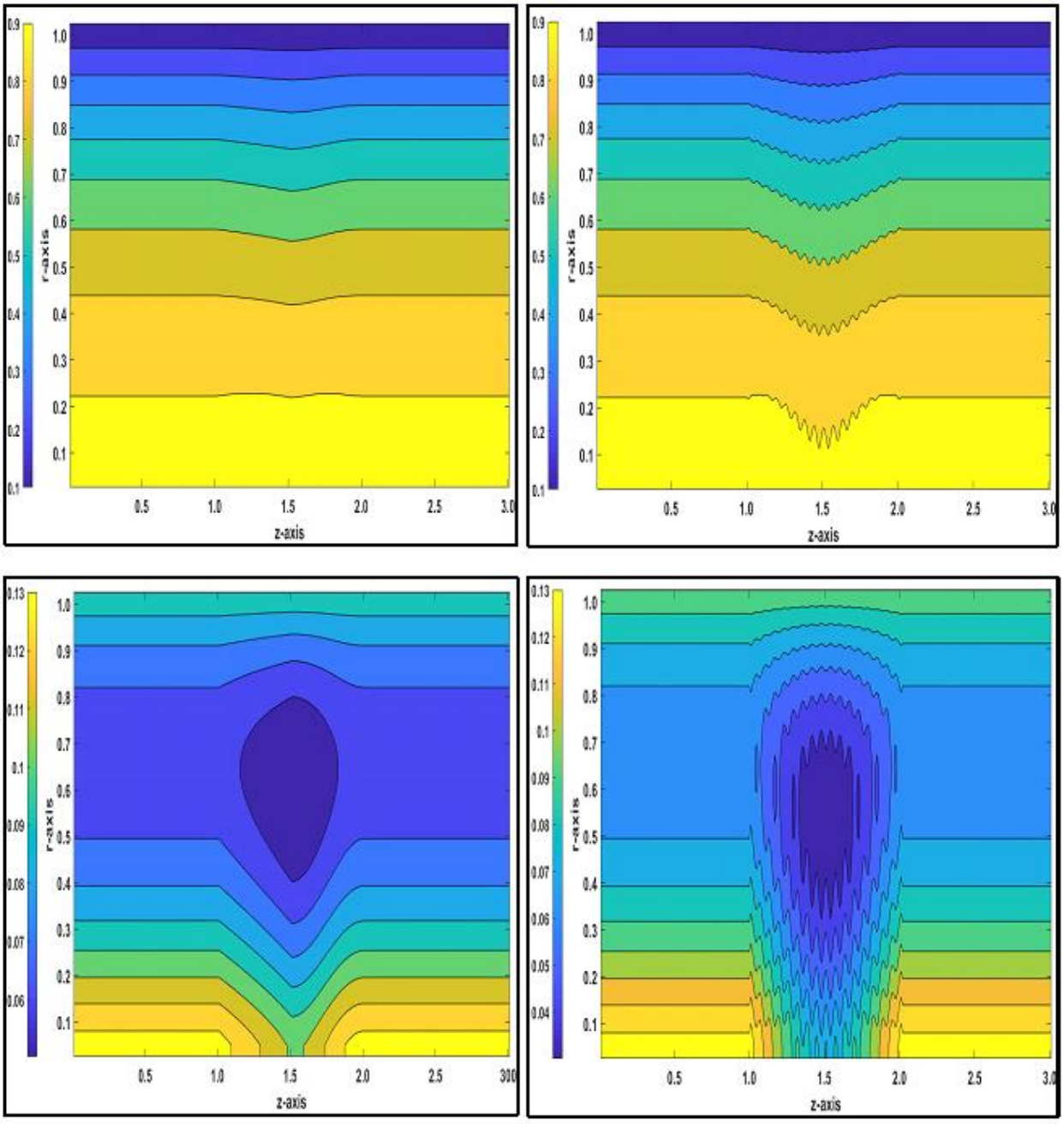

Figure 30: Blood Flow pattern along the axial direction with the following data

(b) For pure blood (ϕ=0.00) through composite and irregular stenoses and for *n=1.5, n=0.5* respectively

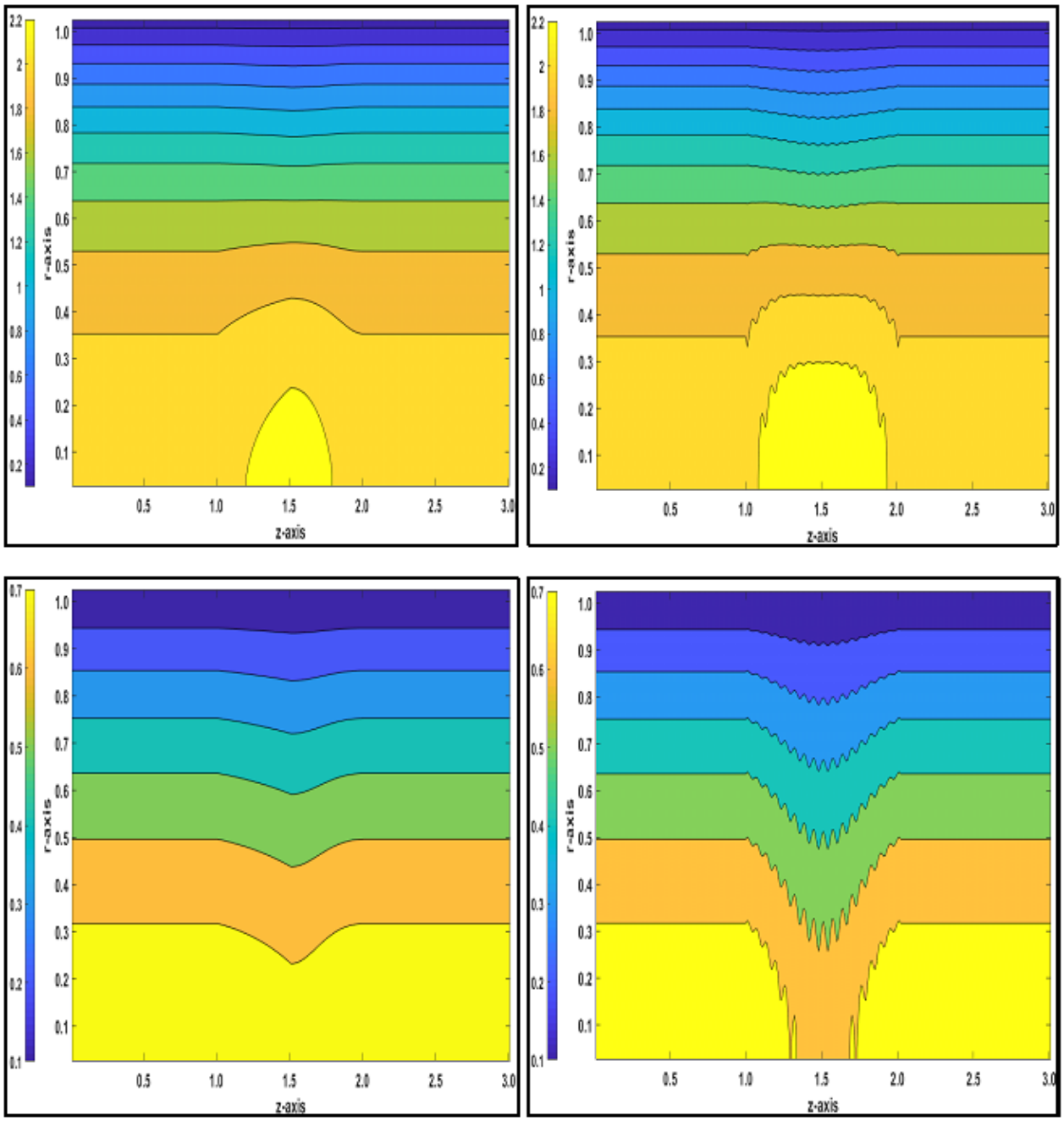

Figure 30: Blood Flow pattern along the axial direction with the following data

(c) For without magnetic parameter (M=0) through composite and irregular stenoses and for n=1.5, n=0.5 respectively

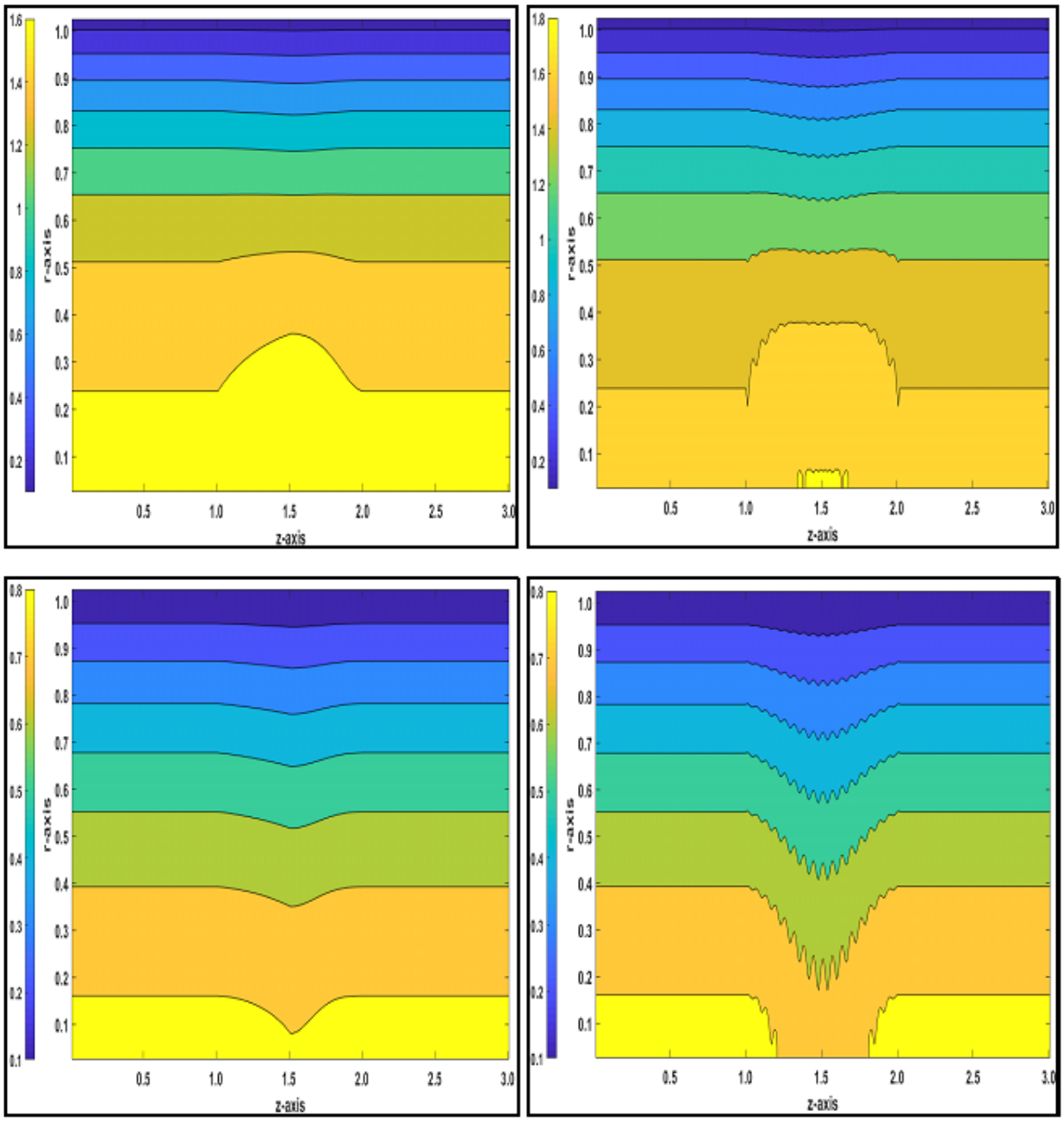

Figure 30: Blood Flow pattern along the axial direction with the following data

(d) For higher Weissenberg number (*We*=3.5) through composite and irregular stenoses and for *n*=1.5, *n*=0.5 respectively

Thermophysical properties	***ρ (Kg/m³)***	***K (W/m-K)***	***γ x 10⁻⁵ (K⁻¹)***	***C_p (J/Kg-K)***	***σ (S / m)***
Blood *(f)*	1063	0.492	0.18	3594	6.67×10^{-1}
Nanoparticle *(Cu)*	8933	400	1.67	385	5.96×10^{7}

Table 1: Thermophysical properties of blood and nanoparticles [27]

Radius	**Ijaz and Nadeem [46]** ***ϕ=0.00, δ=0.01***	**Present results**	**Ijaz and Nadeem [46]** ***ϕ=0.02, δ=0.01***	**Present results**
0.1	0.00	0.00	0.000	0.000
0.2	0.0317	0.0319	0.0645	0.0649
0.3	0.0418	0.0422	0.0820	0.0826
0.4	0.0420	0.0425	0.0776	0.0782
0.5	0.0366	0.0369	0.0613	0.0618
0.6	0.0283	0.0288	0.0390	0.0394
0.7	0.0191	0.0199	0.0152	0.0181
0.8	0.0109	0.0110	-0.0060	0.0064
0.9	0.0052	0.0055	-0.0206	-0.0210
1.0	0.0039	0.0039	-0.0248	-0.0248

Table 2: Comparison of FTCS code results with Ijaz and Nadeem [46] for axial velocity at throat of stenotic artery $z = 1.5$ and $t = 1.2$

Parameter	***ϕ***	***B_1***	**W_b**	**α**	***Gr_T=Gr_N***	***Pr***	***Re***	***Le***	***Nb***	***Nt***	***M***	***We***
Value	0.03	1.41	0.1	0.1	2	14	2	2	0.3	0.3	1	2.5

Table 3: Default value of emerging parameters implemented in FTCS simulations

Nb variation	Nt variation	Composite Stenosis		Irregular Stenosis	
		n=1.5	n=0.5	n=1.5	n=0.5
0.1	0.1	3.028584277	1.054112418	3.0537867	0.989232198
	0.3	6.527871622	2.938486635	6.67247306	2.75087741
	0.5	10.00981999	4.816168309	10.27212639	4.50341293
0.3	0.1	1.861258313	0.42590075	1.846111827	0.401226285
	0.3	3.034468979	1.057133953	3.058820242	0.991307471
	0.5	4.202018947	1.686196952	4.265292935	1.57840247
0.5	0.1	1.62779312	0.300258417	1.604576853	0.283625103
	0.3	2.335788451	0.680863416	2.336089678	0.639393483
	0.5	3.040458739	1.06020268	3.063926244	0.993400379

Table 4: Volumetric flow rate for various emerging parameters considering n = 1.5 and n = 0.5 at time t=1.0